WILEY-VCH

# Supporting Information

## Ultrathin, Layer-by-Layer Assembled Lithiophilic Interlayers for Dendritic Growth-Suppressed Lithium Metal Anodes

*Donghyeon Nam[§], Kyuho Jin[§], Tae Hwan Jo[§], Chanseok Lee, Keun Hee Kim, Hyewon Kang, Ho Yeon Jang, Younghoon Kim, Seung Woo Lee, Seoin Back* Yongmin Ko* Jinhan Cho**

D. Nam, C. Lee, Prof. J. Cho

Department of Chemical and Biological Engineering, Korea University, 145 Anam-ro, Seongbuk-gu, Seoul 02841, Republic of Korea.

E-mail: jinhan71@korea.ac.kr

K. Jin, Prof. J. Cho, Prof. S. Back

KU-KIST Graduate School of Converging Science & Technology, Korea University, 145 Anam-ro, Seongbuk-gu, Seoul 02841, Republic of Korea

E-mail: sback@korea.ac.kr

T. H. Jo, H. Y. Jang

Department of Chemical and Biomolecular Engineering, Sogang University, Baekbeom-ro 35, Mapo-gu, Seoul 04107, Republic of Korea.

K. H. Kim, H. Kang, Prof. S. W. Lee

The George W. Woodruff School of Mechanical Engineering, Georgia Institute of Technology, Atlanta, Georgia 30332, USA

Prof. Y. Kim

Department of Chemistry, Kookmin University, 77 Jeongneung-ro, Seongbuk-gu, Seoul 02707, Republic of Korea

Y. Ko

Division of Energy & Environmental Technology, Materials Research Institute, Daegu Gyeongbuk Institute of Science and Technology (DGIST), 333 Techno Jungang-daero,

Hyeonpung-eup, Dalseong-gun, Daegu 42988, Republic of Korea.

E-mail: yongmin.ko@dgist.ac.kr

Prof. J. Cho

Soft Hybrid Materials Research Center, Advanced Materials Research Division, Korea Institute of Science and Technology (KIST), Seoul 02792, Republic of Korea

[§]These authors equally contributed to this work.

## Experimental Section

**Materials:** Pristine **multiwalled-carbon-nanotubes (MWCNTs) and** tris(2-aminoethyl) amine (TAA) were purchased from MERCK. Carboxylic acid (COOH) functionalization of the pristine MWCNTs was conducted by oxidizing them with an $H_2SO_4/HNO_3$ mixture at 70°C for 2 h. The resulting suspension was then carefully washed using dialysis tubing to eliminate the byproducts and residuals. Organic solvents (ethanol, acetone) were obtained from Daejung Chemicals & Metals (Republic of Korea). The other chemical reagents were purchased from Sigma−Aldrich and used without further purification.

**Fabrication of multiwalled-carbon-nanotube-forest (MWCF):**

As-prepared COOH-MWCNTs and $NH_2$-TAA molecules were dispersed in ethanol at concentrations of 1 mg $mL^{-1}$ each. To build the $(NH_2\text{-TAA/COOH-MWCNT})_n$ multilayers (MWCF), one side of the substrate (Celgard 2400 separator, quartz, or silicon wafer) was subjected to UV-ozone treatment for 5 minutes to introduce oxygen-containing functional groups on the surface. The substrate was then first immersed in the $NH_2$-TAA solution for 10 minutes to form an $NH_2$-TAA layer through hydrogen-bonding interactions, and the weakly adsorbed TAA molecules were subsequently washed out with pure ethanol. The $NH_2$-TAA-coated substrate was then dipped into the COOH-MWCNT solution for 10 minutes and washed with pure ethanol. This procedure was repeated to obtain the *n*−MWCF with the desired bilayer number (*n*).

**Preparation of $LiFePO_4$ (LFP) and $LiNi_{0.8}Mn_{0.1}Co_{0.1}O_2$ (NMC811) Cathodes:**

The cathode preparation involved mixing either LFP or NMC811 powder with Super P carbon and PVDF binder in a weight ratio of 8:1:1. This mixture was dispersed in NMP to form a uniform slurry. The slurry was then coated onto carbon-coated aluminum foil (18 μm thick) using a doctor blade and dried at 90°C overnight. After the drying process, the cathode sheets were pressurized at 20 MPa for 1 min.

**Cell Assembly and Electrochemical Measurements:**

Electrochemical measurements were performed using CR2032-type coin cells (MTI Corporation) and a WBCS3000 multichannel workstation. The cells were assembled in an argon-filled glovebox (MBraun, $O_2$ < 0.1 ppm, $H_2O$ < 0.1 ppm), with Li foil (35 μm thick) as the anode, the prepared cathode, and either a Celgard 2400 separator or the n-MWCF separator. For Li | Ni half-cells and Li | Li symmetric cells, the electrolyte used was 1 M LiTFSI in 1,2-dimethoxyethane (DME)/1,3-dioxolane (DOL) (1:1 by vol%) with 2 wt% $LiNO_3$. For Li | NMC811 and Li | LFP cells, the electrolyte was 1 M $LiPF_6$ in ethylene carbonate (EC)/diethyl carbonate (DEC) (1:1 by vol%). For all coin cells, the amount of electrolyte was fixed at 100 μL. The galvanostatic charge-discharge tests for Li | NMC811 cells were conducted in the potential range of 2.7 to 4.3 V at 0.1 C for the first two cycles, followed by subsequent cycles at varying rates. Li | LFP cells were tested in the range of 3.5 to 4.0 V under similar conditions. The theoretical capacity of NMC811 and LFP used for the C-rate calculation was 200 and 170 mAh $g^{-1}$, respectively. Li | Ni cells were cycled at a current density of 1 mA $cm^{-2}$ with a cut-off voltage of 1.0 V. Electrochemical impedance spectroscopy (EIS) measurements were performed over a frequency range of 100 kHz to 0.1 Hz with a perturbation amplitude of 0.01 mV. All electrochemical tests were performed at room temperature (25°C). Electrochemical

tests were conducted using at least three independent cells for both symmetric and asymmetric configurations to ensure performance reliability.

**Pouch Cell Assembly:**

The pouch cells were assembled in an argon-filled glovebox (MBraun, $O_2$ < 0.1 ppm, $H_2O$ < 0.1 ppm). First, the Al and Ni tabs of the cathode and anode, respectively, were welded using an ultrasonic welder (GN−800, Gelon). After the welding, the 20 μm-thick Li-coated Cu foil (11μm thick), 3−MWCF separator, and as-prepared cathode were packed into a laminate bag and filled with the electrolyte. Then, the laminated bag was finally vacuum sealed.

**Characterization:**

High-resolution transmission electron microscopy (HR-TEM) was performed using a Technai 20 instrument (FEI). Field-emission scanning electron microscopy (FE-SEM) was conducted with a Hitachi S-4800 instrument. The adsorption behavior and surface functionality of LbL-assembled multilayers were investigated using a Fourier transform infrared (FTIR) spectroscopy. This analysis was carried out with a CARY 600 spectrometer (Agilent Technologies) in specular mode, with a resolution of 4 $cm^{-1}$ at room temperature under ambient conditions. The data obtained from 200 scans were processed using OMNIC software (Nicolet). The UV-vis spectra of the LbL-assembled multilayers were measured using a Lambda 35 instrument (Perkin Elmer). X-ray photoelectron spectroscopy (XPS) was carried out using an X-TOOL system (ULVAC-PHI). Quartz crystal microgravimetry (QCM) analysis was performed using a QCM200 (SRS) device. The mass of each layer of the ($NH_2$-TAA/COOH-

MWCNT)$_n$ multilayers (MWCF) was calculated from the frequency changes during the LbL deposition process using the simplified Sauerbrey equation:[S1]

$$\Delta F\ (Hz) = -56.6 \times \Delta m$$

Here, $\Delta F$ *and* $\Delta m$ represent the frequency and mass changes, respectively, for each layer of the ($NH_2$-TAA/COOH-MWCNT)$_n$ multilayers. The Brunauer-Emmett-Teller (BET) pore size distribution and specific surface areas of n-MWCF-coated separator were measured using $N_2$ (99.999%) adsorption at 77 K (BELSORP-mini II, MicrotracBEL, Corp).

**Computational Details :**

All calculations were performed using Q-Chem code version 5.4.0,[S2] employing B3LYP (Becke three-parameter hybrid functional combined with Lee–Yang–Parr) correlation functional[S3] with a 6-311++G(d, p) basis set.[S4] We modelled Celgard, H-terminated molecular graphene with and without the carboxyl (−COOH) group and conducted structural optimization using the Direct Inversion in Iterative Subspace (DIIS) algorithm with the convergence threshold of $10^{-7}$ a.u.. Using the optimized structures, we investigated various Li adsorption configurations, and the representative adsorption configurations.

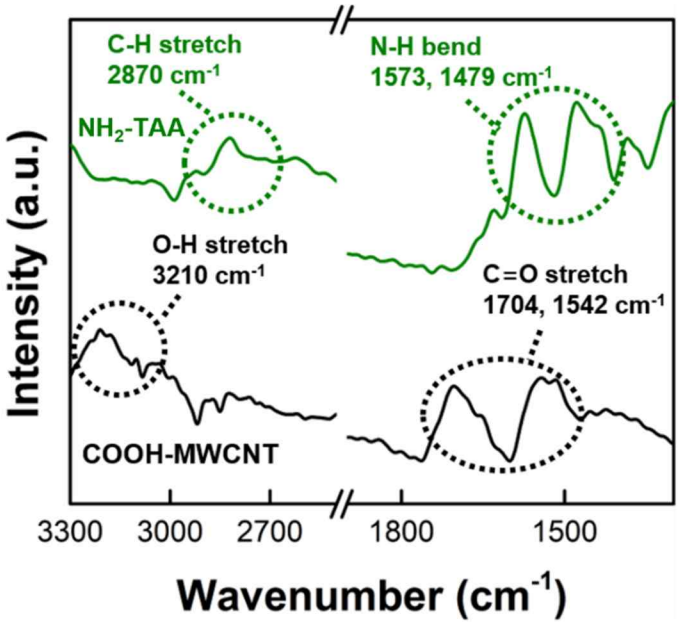


**Figure S1.** FTIR spectra of, COOH−MWCNT (black solid-line), and $NH_2$−TAA (green solid-line). Strong absorption peaks originating from O−H and C=O stretching vibrations of COOH groups appeared, indicating that the COOH groups are well-anchored on the MWCNT surface (COOH−MWCNT).

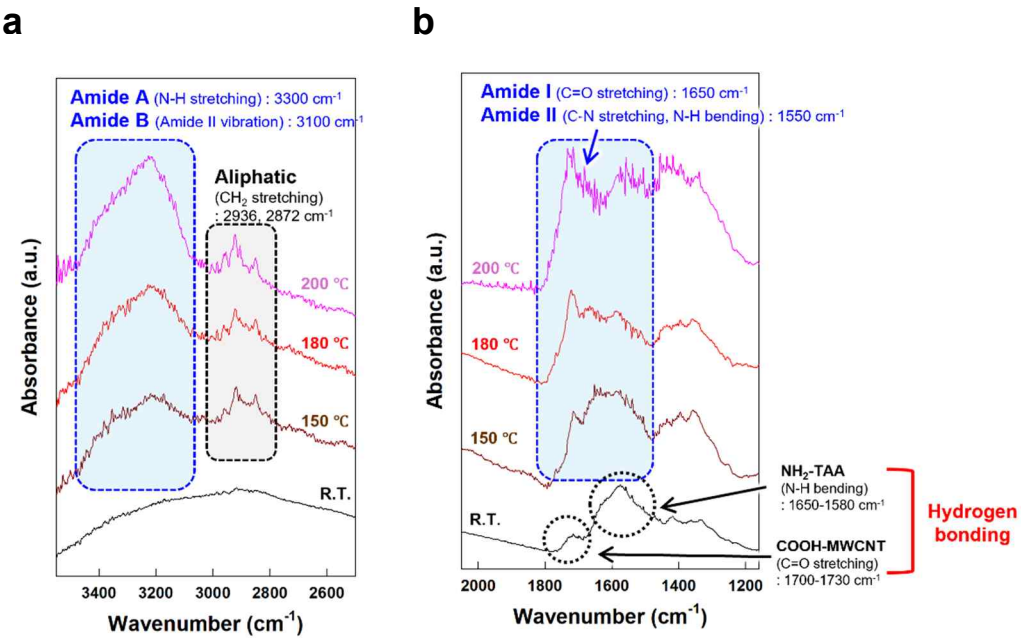


**Figure S2.** FTIR spectra of (COOH-MWCNT/$NH_2$-TAA)$_n$ multilayers were analyzed before and after thermal treatment (at 150, 180 , and 200℃) for 3 h in region of a) 2500-3550 $cm^{-1}$ and b) 1150-2050 $cm^{-1}$. After thermal treatment, distinct amide bonds were observed in the (COOH−MWCNT/$NH_2$−TAA)$_n$ multilayers, confirming the successful conversion of hydrogen bonds to amide bonds. This result clearly demonstrates that the multilayers are assembled through hydrogen-bonding interactions between the COOH and $NH_2$ groups.

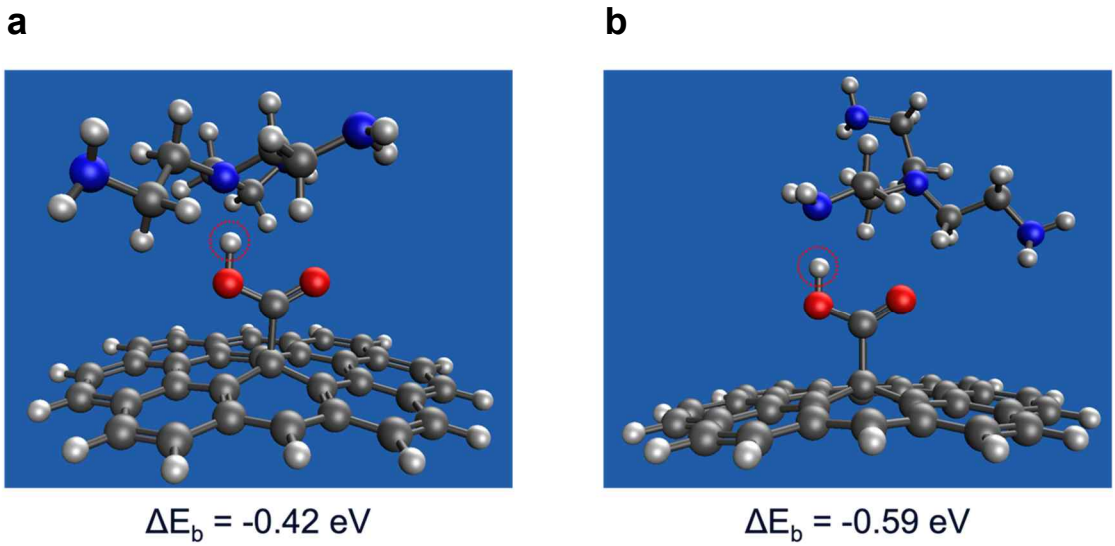


**Figure S3**. Atomic structures demonstrating interactions between COOH group and a) tertiary N and b) primary amine group of $NH_2$−TAA. Color codes: blue (nitrogen, N), white (hydrogen, H), grey (carbon, C). In this case, the DFT results evidently demonstrated that the binding energy between primary amine ($NH_2$) of $NH_2$−TAA and COOH groups of COOH−MWCNTs (−0.59 eV) is stronger than that between tertiary N of $NH_2$−TAA and COOH groups of COOH−MWCNTs (−0.42 eV).

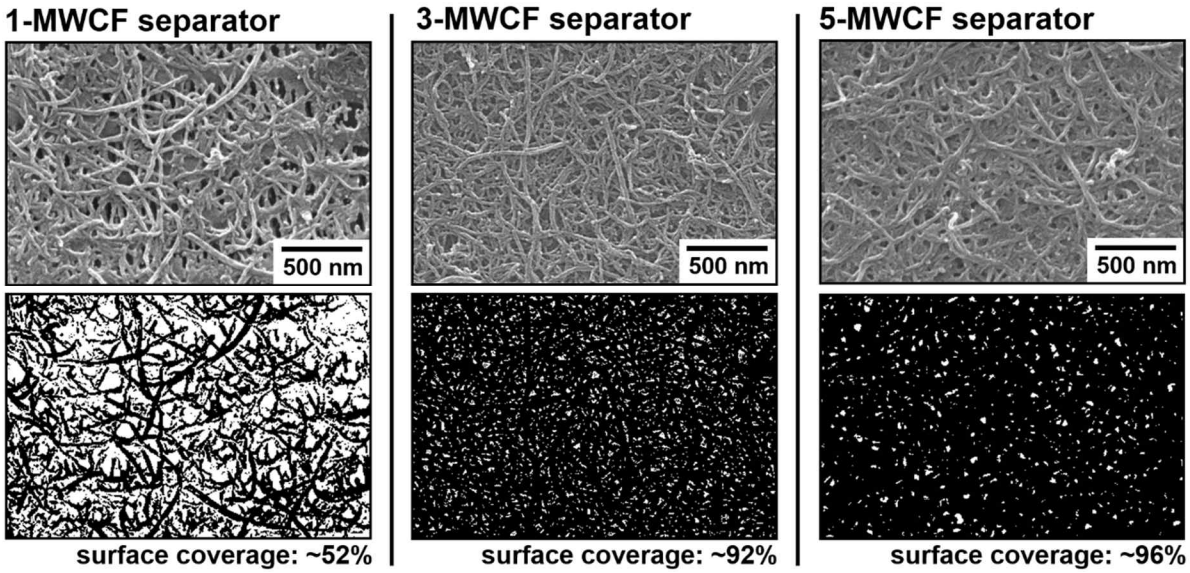


**Figure S4.** Surface coverage analysis. FE-SEM images (top) of each *n*−MWCF separator and corresponding binary images (bottom) for visualizing surface coverage of the MWCF on the separator. These results were obtained by ImageJ software.[S5] In this case, the depicted binary images of each *n*−MWCF separator represent the coverage on the PP separator (Celgard 2400), rather than the porosity of the MWCF itself.

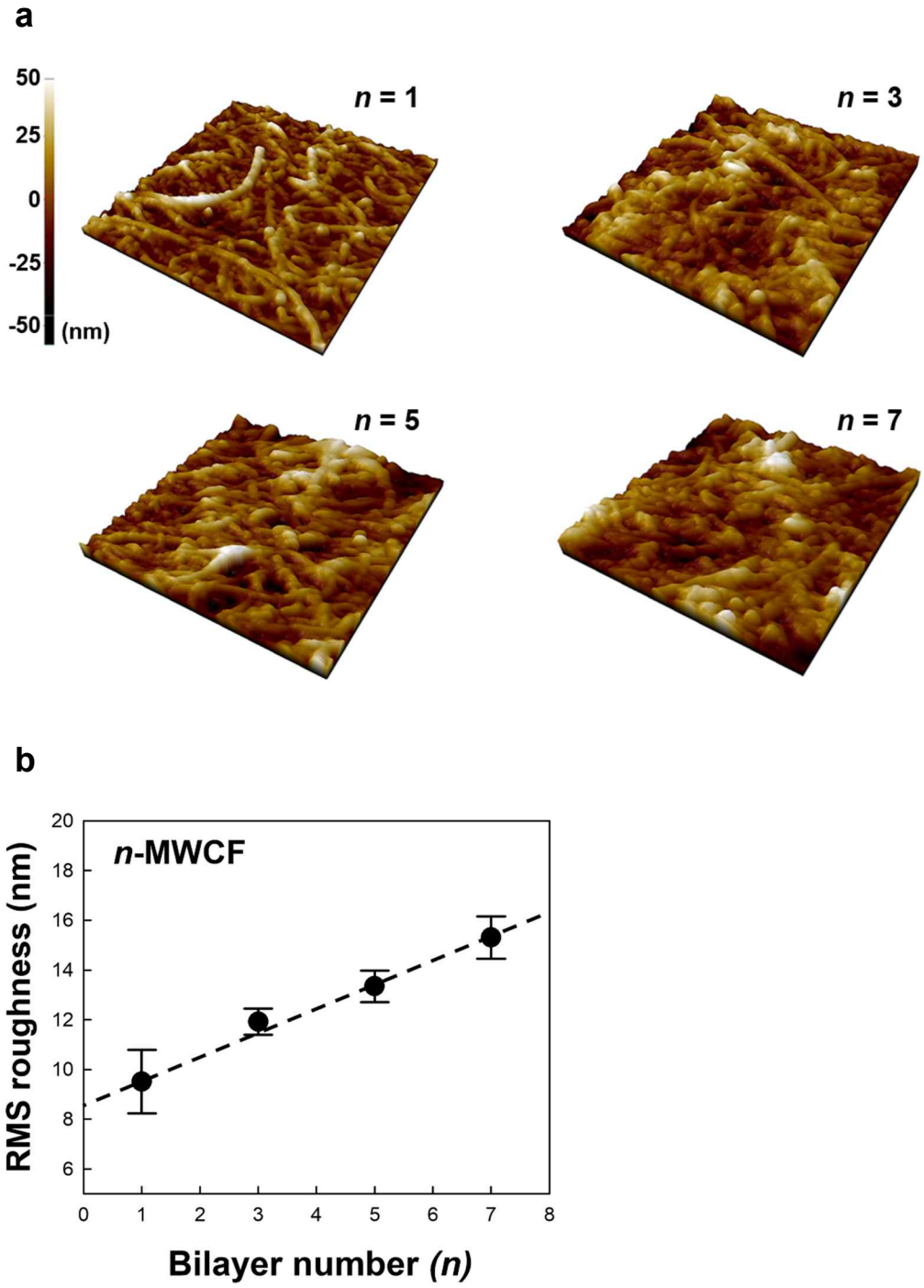


**Figure S5.** Surface morphology of *n*-MWCF. a) AFM topographic images of *n*−MWCFs (i.e., $NH_2$−TAA/COOH−MWCNT multilayers) coated onto the Si wafer substrate with different bilayer number (*n*) of 1, 3, 5, and 7. b) Root mean square (RMS) roughness values of MWCFs on the Si water substrate as a functional of bilayer number (*n*). In this case, the RMS roughness was measured to be 9.5±1.3, 11.9±0.5, 13.3±0.6, and 15.3±0.8 for 1, 2, 5, and 7−bilayered MWCFs, respectively.

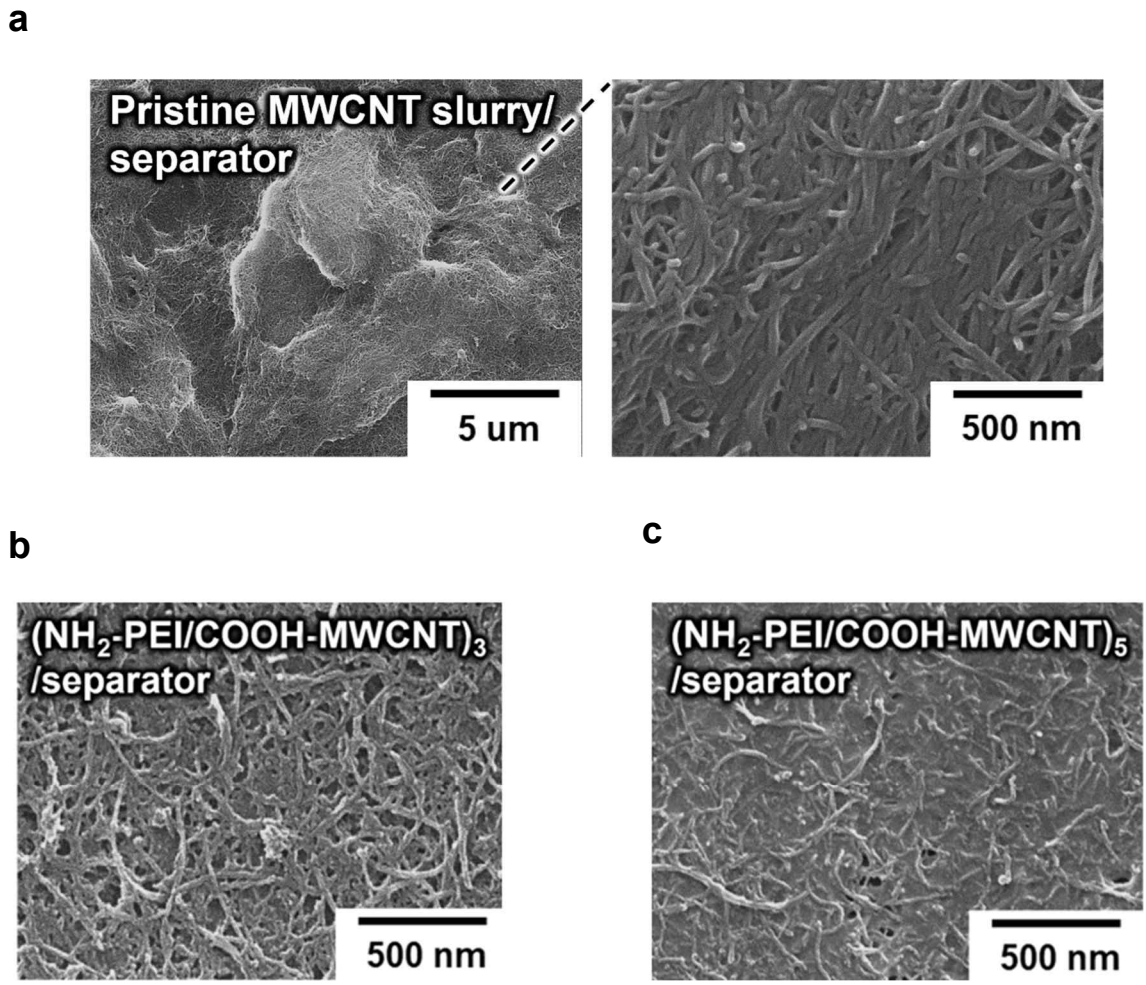


**Figure S6.** Surface morphologies of polymer binder-employed MWCNT interlayers. FE-SEM images of a) pristine MWCNT slurry with PVDF binder coated onto the separator. FE-SEM images for $(NH_2-poly(ethyleneimine)/COOH-MWCNT)_n$-coated separators with a different bilayer number ($n$) of b) 3 and c) 5, respectively.

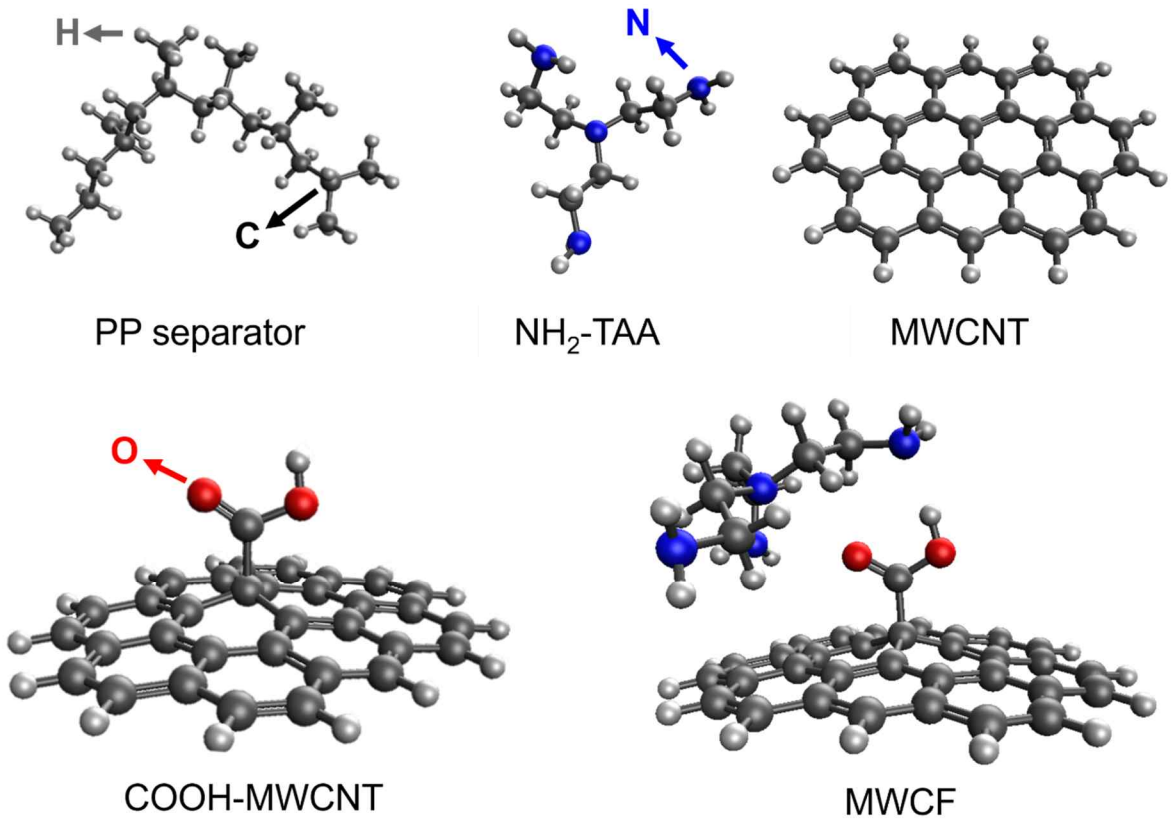


**Figure S7.** Representative chemical structures of PP separator (Celgard 2400), $NH_2$−TAA, pristine MWCNT, COOH−MWCNT, and MWCF, respectively.

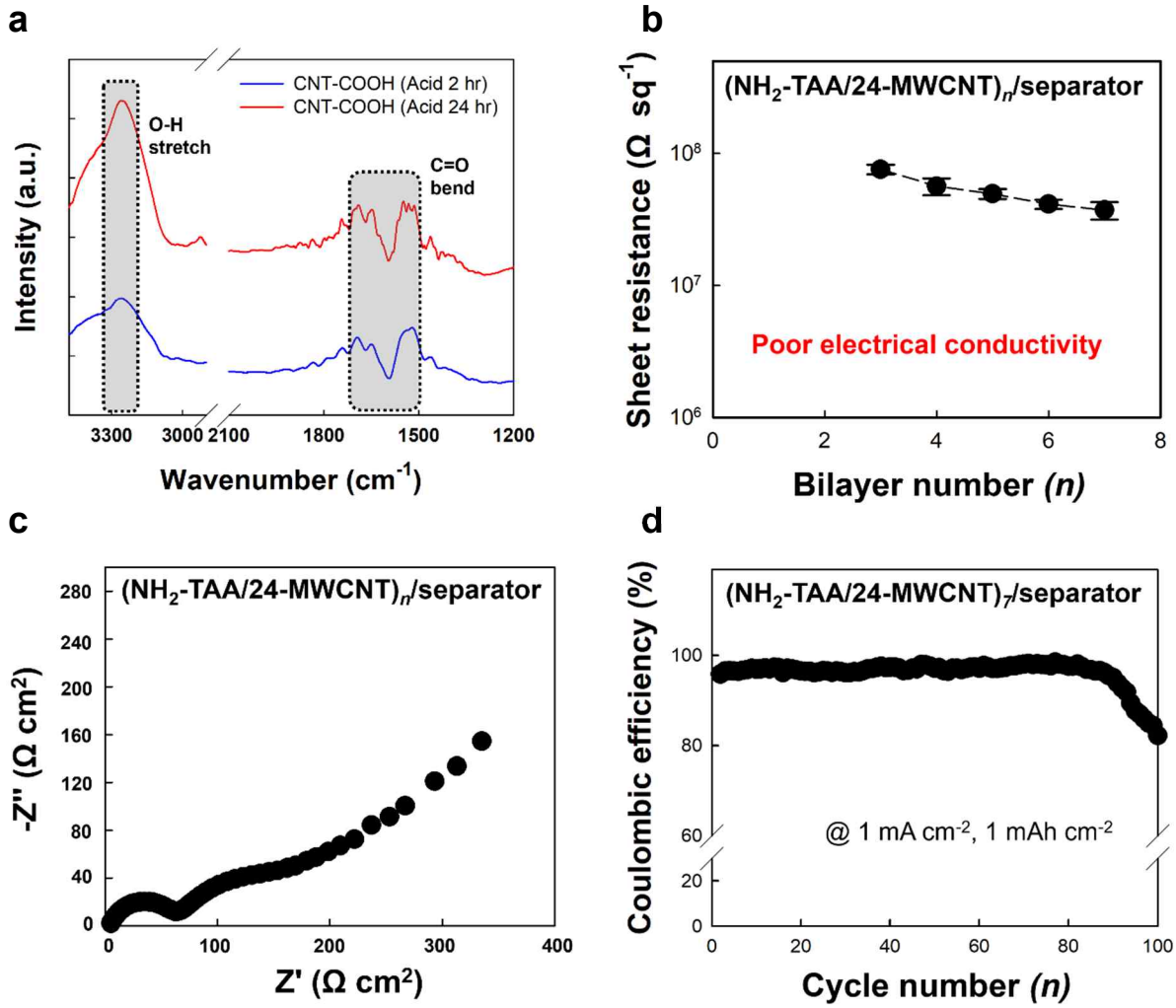


**Figure S8.** 24-hour acid-treated MWCNTs. a) FTIR spectra of COOH−MWCNTs with a different oxidation time. The MWCNTs with a 24−hour acid treatment (abbreviated as 24−MWCNT) exhibited approximately 2.4 times higher content of oxidation groups compared to the 2-hour treated one. This value was estimated by monitoring the change in the peak intensity of C=C bond vibration. b) Bilayer number ($n$)-dependent sheet resistance of ($NH_2$-TAA/24−MWCNT)$_n$ multilayers. The sheet resistance value of 3-bilayered film was measured to be $3.7 \times 10^7$ Ω $sq^{-1}$. c) Nyquist plot and d) cycling stability test of ($NH_2$-TAA/24-MWCNT)$_7$ multilayer-coated separator-based Li | Ni half-cells. In this case, the cell showed the charge transfer resistance ($R_{ct}$) of 32.3 Ω and the equivalent-series resistance ($R_s$) of 1.09 Ω. Additionally, the Coulombic efficiency (CE) was retained as 82.2 % up to 100 cycles.

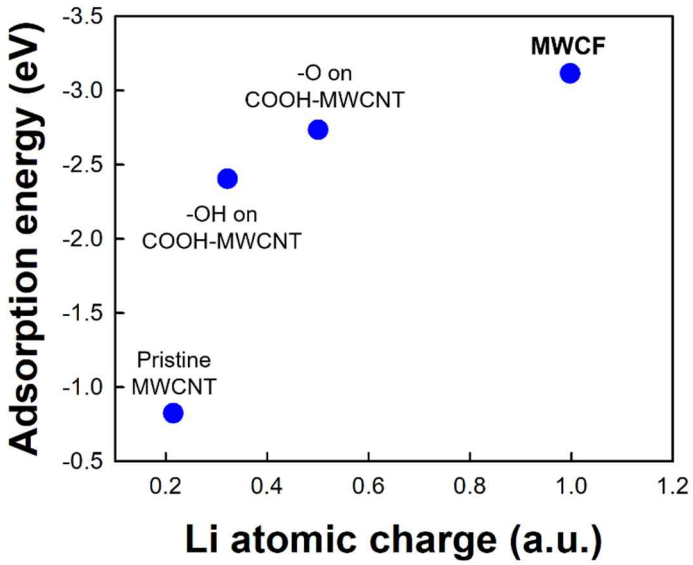


**Figure S9.** Li atomic charge. Atomic charge of Li as a function of functional groups with different adsorption energies. Note that the MWCF contains functional groups of OH, O, and $NH_2$.

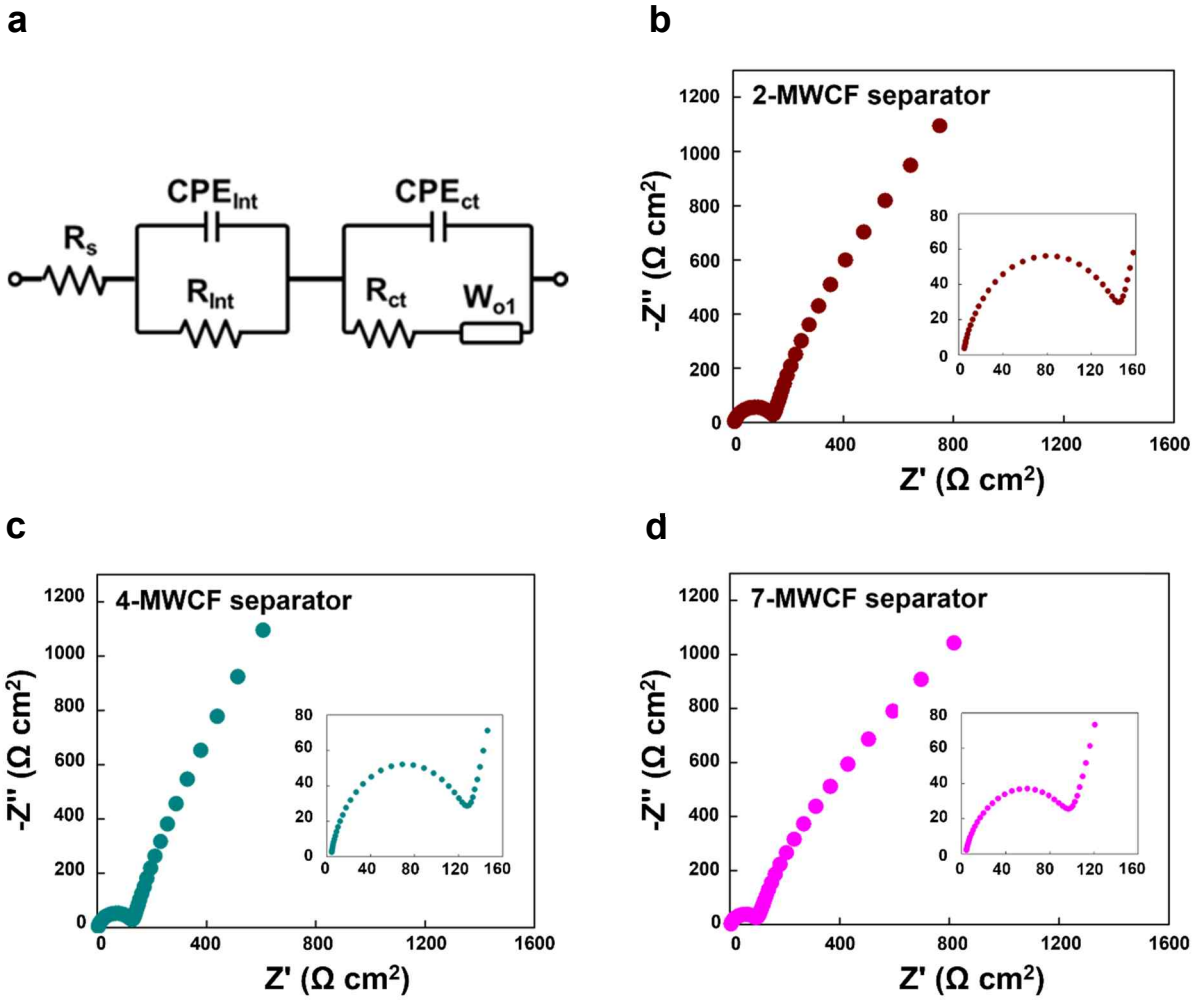


**Figure S10.** Nyquist plots for *n*-MWCF separator-based half-cells. a) Representative equivalent circuit of of *n*−MWCF separator-based half-cell. (B-D) EIS spectra of the Li | Ni half-cells assembled using *n*−MWCF separator with varying bilayer number (*n*): b) $n = 2$, c) $n = 4$, and d) $n = 7$. The insets indicate an enlarged view of the EIS spectrum in the high-frequency region.

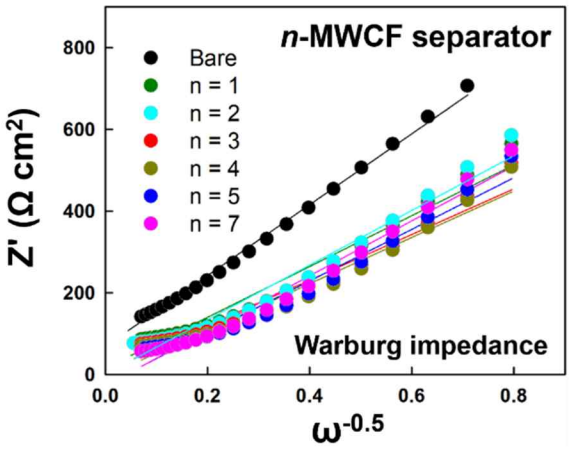


| Bilayer | σω (Warburg impedance) | D ($10^{-14}$ cm$^2$s$^{-1}$) |
|---|---|---|
| 0 | 867.8 | 1.50 |
| 1 | 681.0 | 2.44 |
| 2 | 669.0 | 2.53 |
| **3** | **558.9** | **3.63** |
| 4 | 567.2 | 3.52 |
| 5 | 704.9 | 2.28 |
| 7 | 723.8 | 2.16 |

**Figure S11.** Diffusion kinetics of *n*-MWCF separator. Bilayer number (*n*)-dependent diffusion coefficient of the *n*−MWCF separator-based half-cells calculated from Warburg impedance data from Figure 3b and S10.

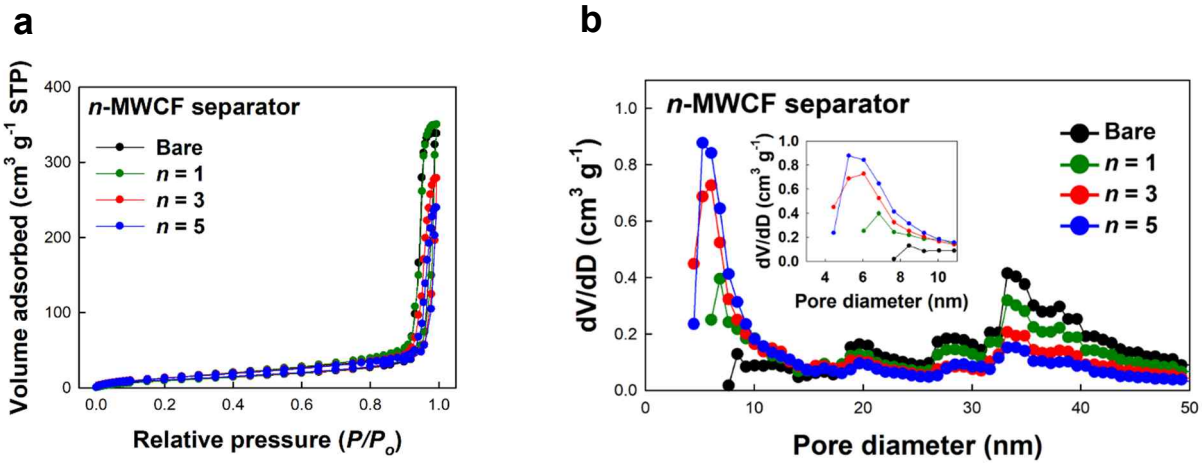


**Figure S12.** BET analysis. a) $N_2$-adsorption-desorption isotherm and b) Comparison of pore size distribution of bare and *n*−MWCF separators (*n* = 1, 3, and 5). The inset illustrates the gradual decrease in pore size of the *n*−MWCFs with increasing bilayer number (*n*).

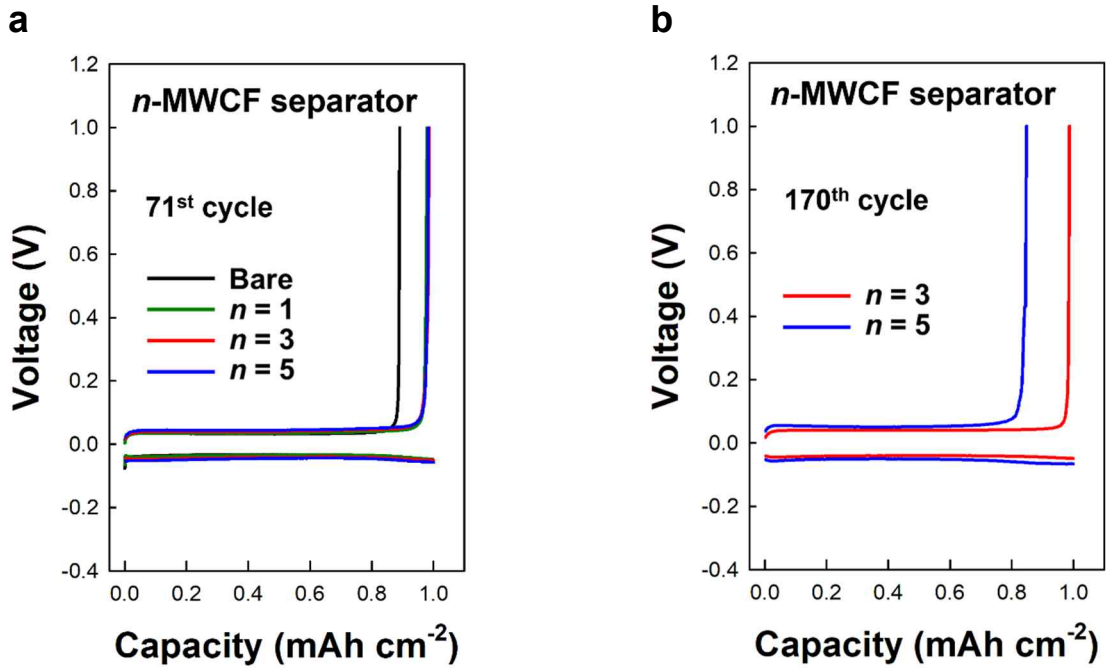


**Figure S13.** Cycle number-dependent voltage profiles. The voltage vs. charge/discharge capacities of the Li | Ni half-cells based on *n*-MWCF separators at the a) 71$^{st}$ and b) 170$^{th}$ cycles, with varying bilayer numbers (*n*).

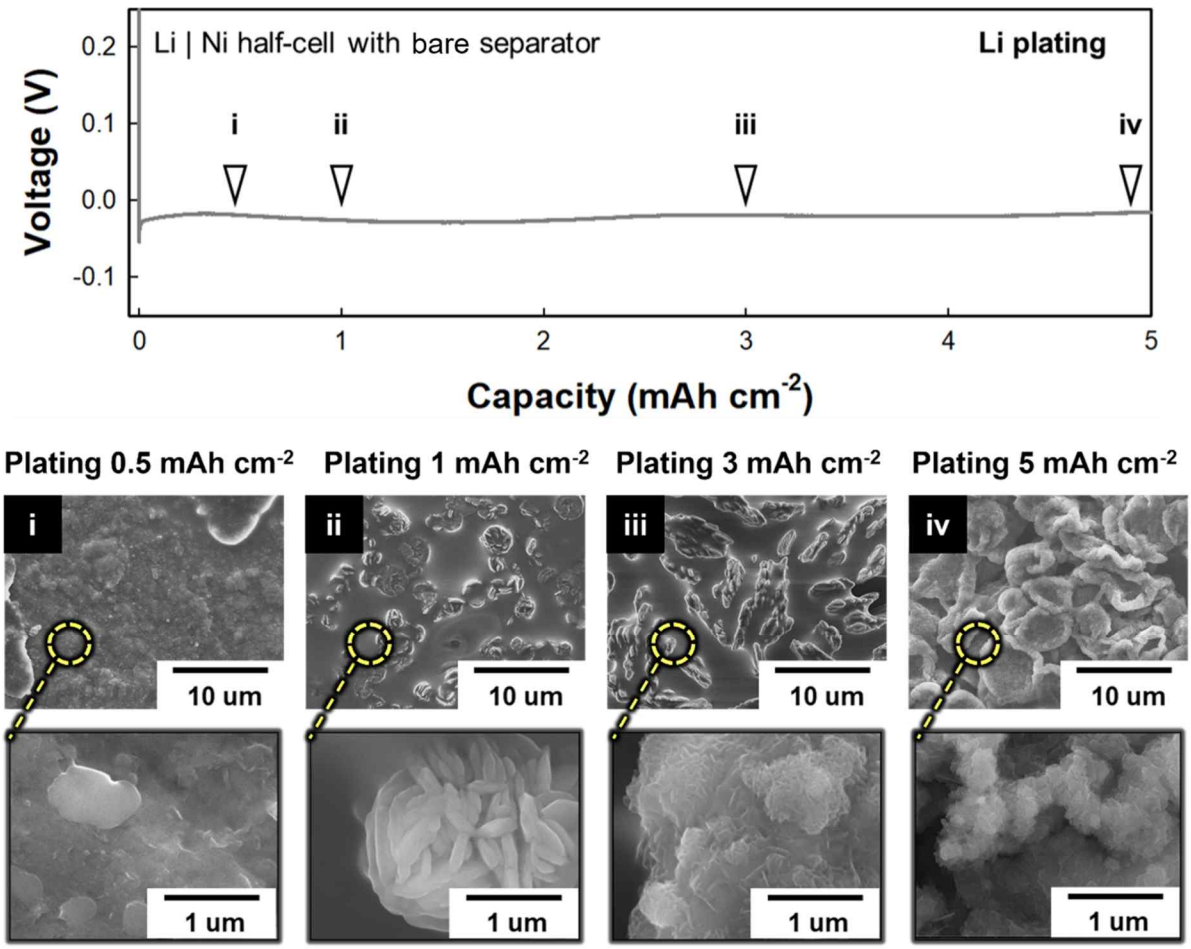


**Figure S14.** Li deposition behavior in bare separator-based cell. Li plating capacity-dependent voltage profile (top) and corresponding FE-SEM images (bottom) of bare separator-based Li | Ni half-cells.

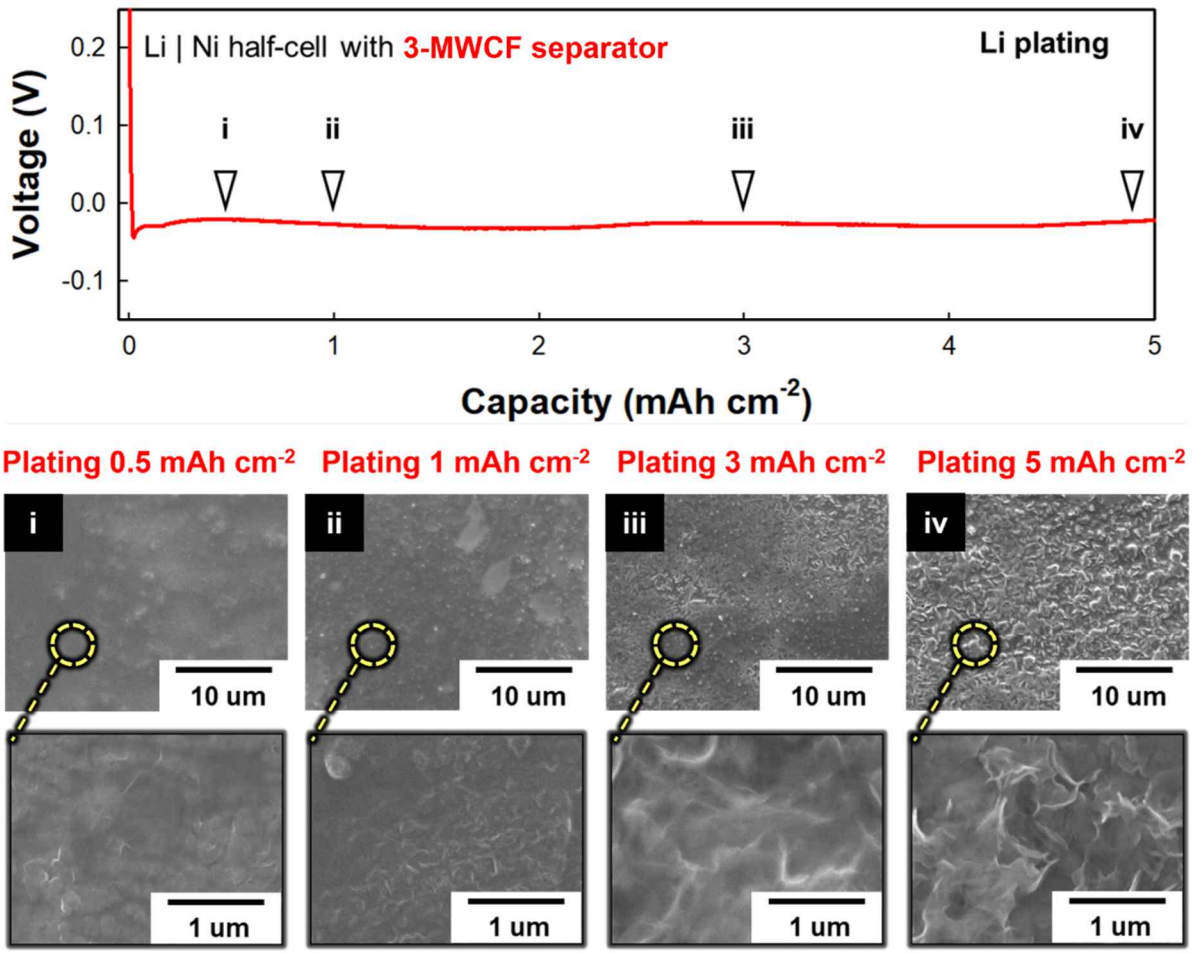


**Figure S15.** Li deposition behavior in 3-MWCF separator-based cell. Li plating capacity-dependent voltage profile (top) and corresponding FE-SEM images (bottom) of 3−MWCF separator-based Li | Ni half-cells.

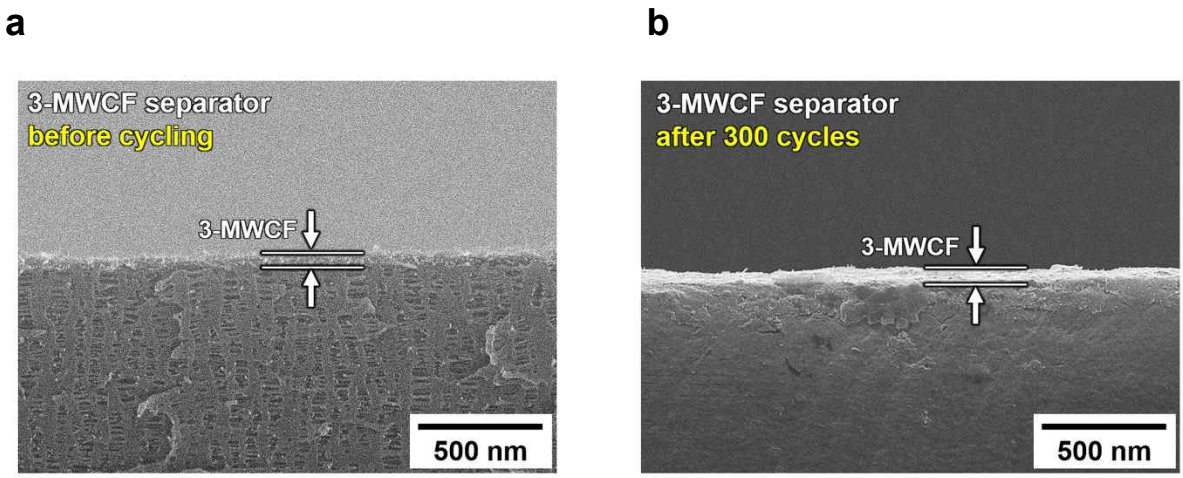


**Figure S16.** Surface morphology. Cross-sectional FE-SEM images of 3−MWCF separator-based cells a) before and b) after 300 cycles. To remove excess electrolytes deposited on the 3-MWCF separator after 300 cycles, the samples were treated with a solvent of 1,2-dimethoxyethane (DME)/1,3-dioxolane (DOL) in a 1:1 by volume ratio. These images confirm that the 3-MWCF layers remain stably deposited onto separator even after prolonged cycling.

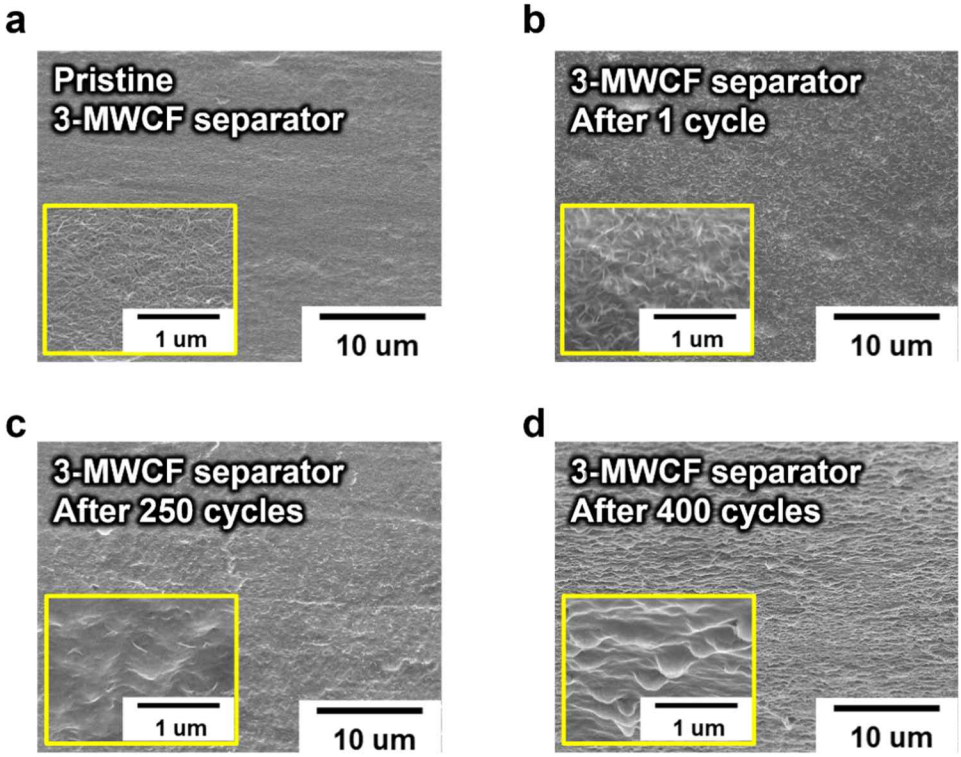


**Figure S17.** Morphology analysis of the 3-MWCF separator. Lithium growth behavior on the 3−MWCF separator in a Li | Li symmetric cell test with different Li plating/stripping cycle numbers: a) 0, b) 1, c) 250, and d) 400 at 3 mA $cm^{-2}$, 1 mAh $cm^{-2}$.

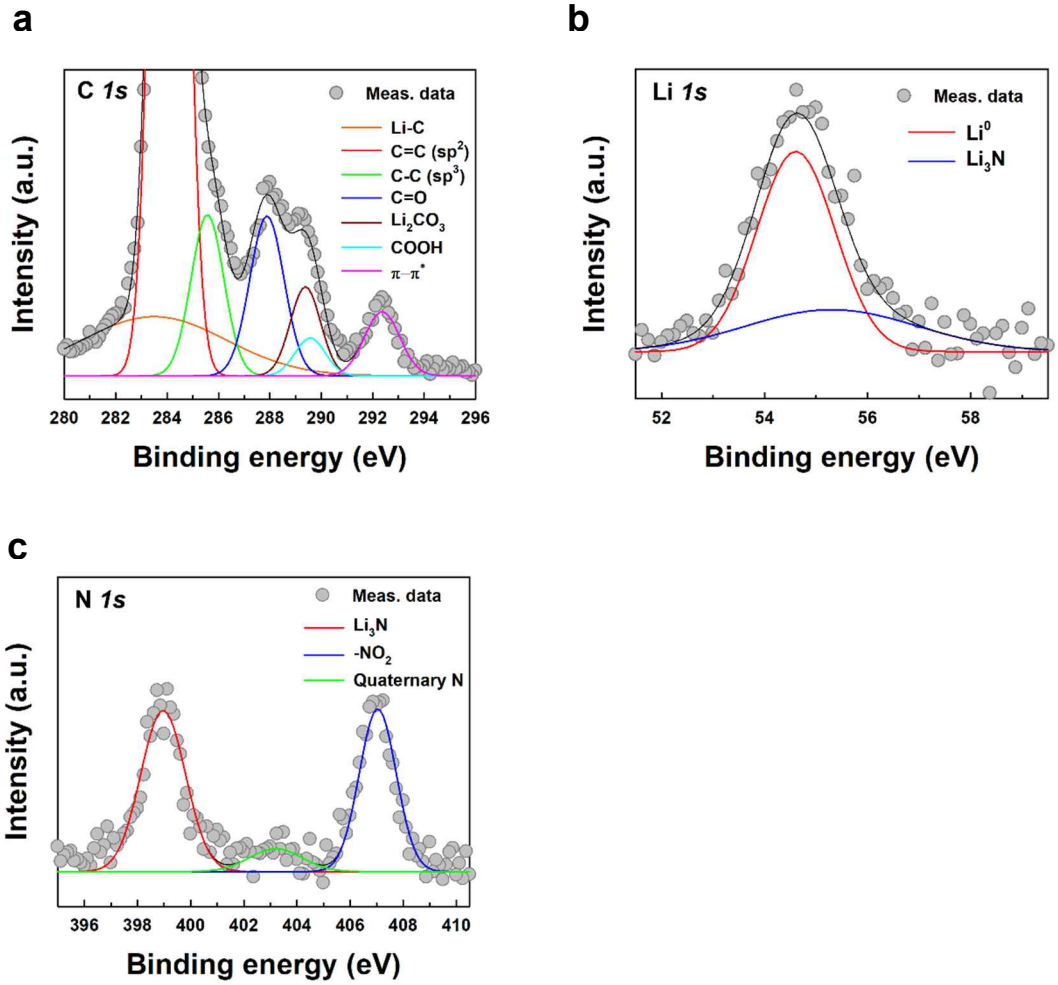


**Figure S18.** XPS analysis of 3-MWCF separator. XPS spectra of a) C *1s*, b) Li *1s* and c) N *1s* for the 3−MWCF separator after discharging step of 400$^{th}$ cycles. The deconvoluted C *1s* spectrum of the 3-MWCF separator showed two distinct peaks corresponding to Li−C bond and $Li_2CO_3$ at 283.5 and 289.5 eV, respectively, indicating the presence of the Li metal and the SEI layer deposited on the MWCF interlayer. The peaks of C=C, C−C, C=O, COOH, and π−π* stacking corresponded to 284.5, 285.1, 288.3, 289.5, and 291.3 eV, respectively, and obviously originate from the COOH−MWCNT of the 3-MWCF separator.[S6]. Additionally, the Li *1s* spectra of the 3−MWCF separator revealed the presence of $Li^0$ (54.8 eV) and $Li_3N$ (55.5 eV), indicating the deposition of Li metal and the SEI layer on the separator. The characteristic peak for SEI layer was also observed clearly in the N *1s* spectrum at 398.6 eV ($Li_3N$).[S7]. These results indicate that the use of the 3−MWCF separator induces the simultaneous and uniform Li growth on both the separator and the anode, thereby significantly enhancing the regulation of dendritic Li growth.

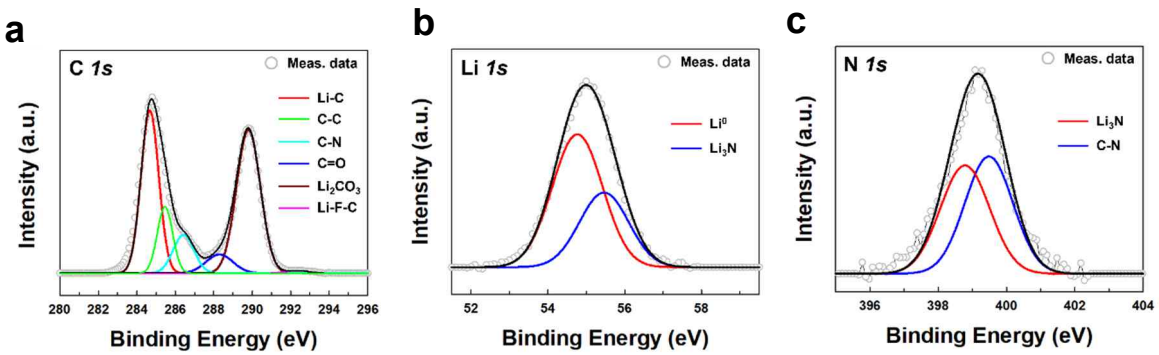


**Figure S19.** XPS spectra of (a) C 1s, (b) Li 1s, and (c) N 1s for the Li metal facing the MWCF interlayer after 400$^{th}$ charge-discharge cycles.

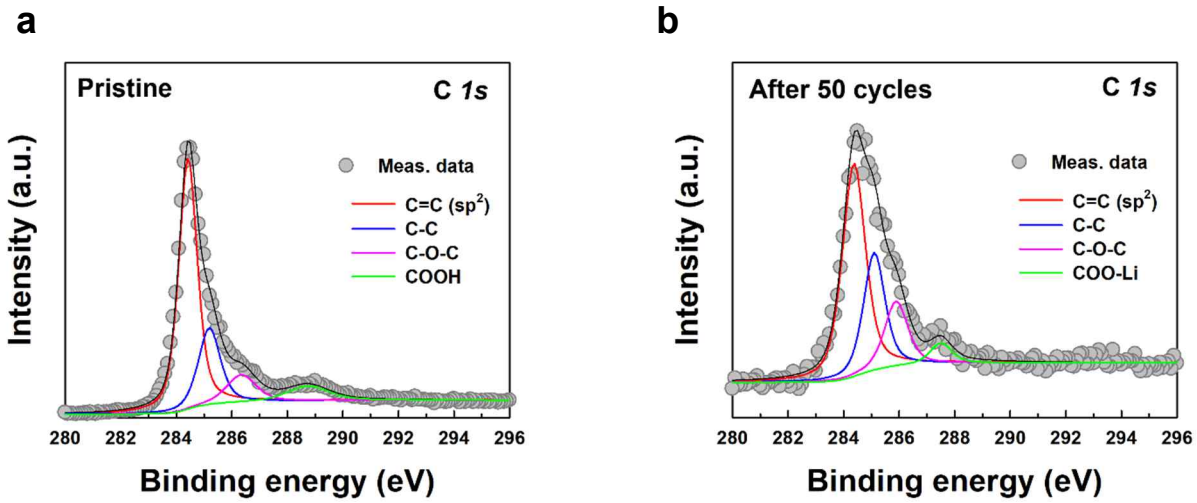


**Figure S20.** C 1s XPS spectra of the 3-MWCF separator obtained from Li ‖ Ni half cells a) before and b) after 50 plating/stripping cycles. To analyze the underlying 3-MWCF interlayer after cycling, the SEI layer formed on the 3-MWCF surface was selectively etched.

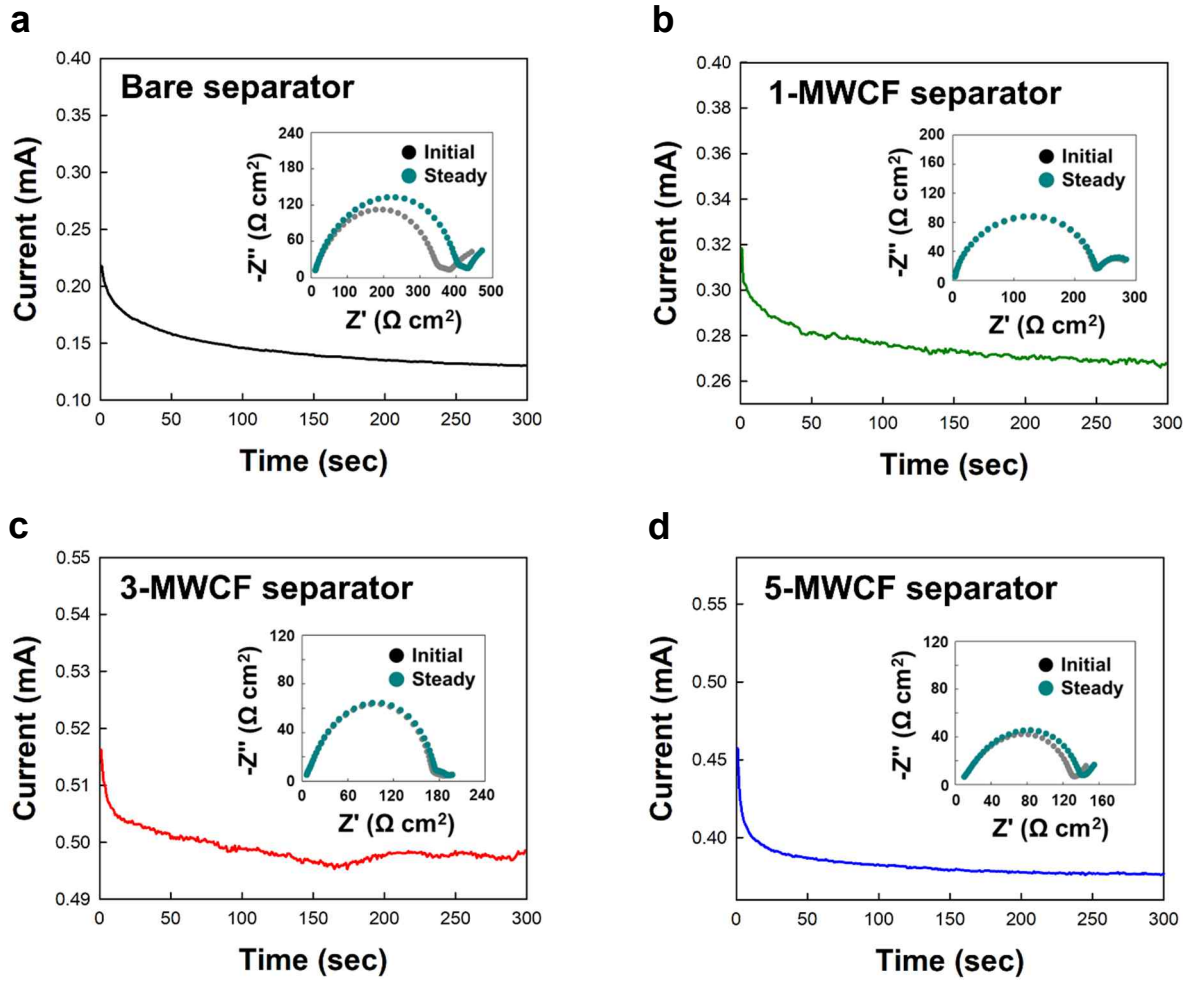


**Figure S21.** Chronoamperometry and EIS measurements. DC polarization profiles and EIS spectra (inset) for *n*−MWCF separator-based Li | Li symmetric cells with different bilayer number (*n*) of a) 0 (bare separator), b) 1, c) 3, and d) 5.

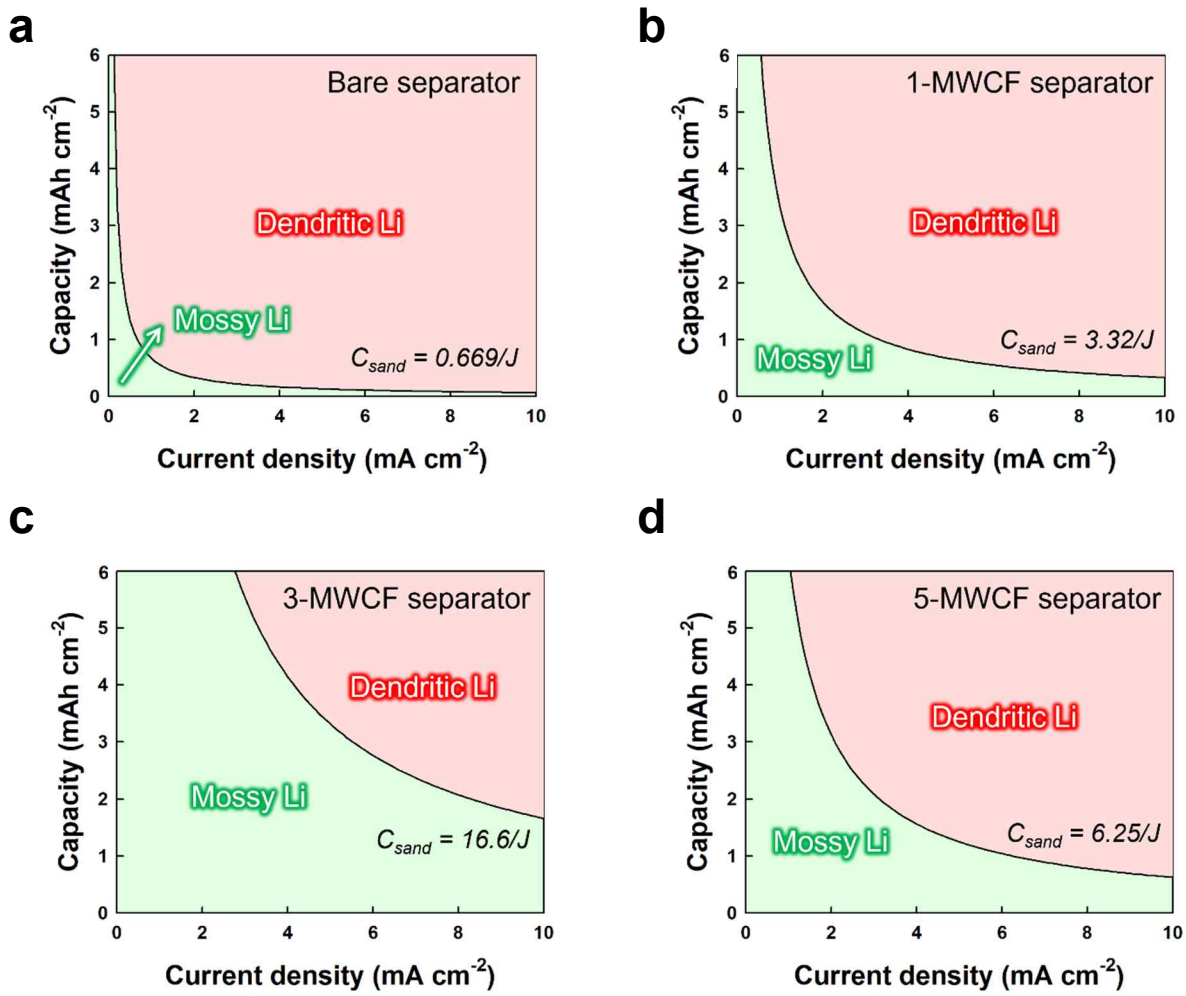


**Figure S22.** Sand's capacity. Current-dependent Sand's capacity of *n*–Janus separator with different bilayer number (*n*) of a) 0, b) 1, c) 3, and d) 5.

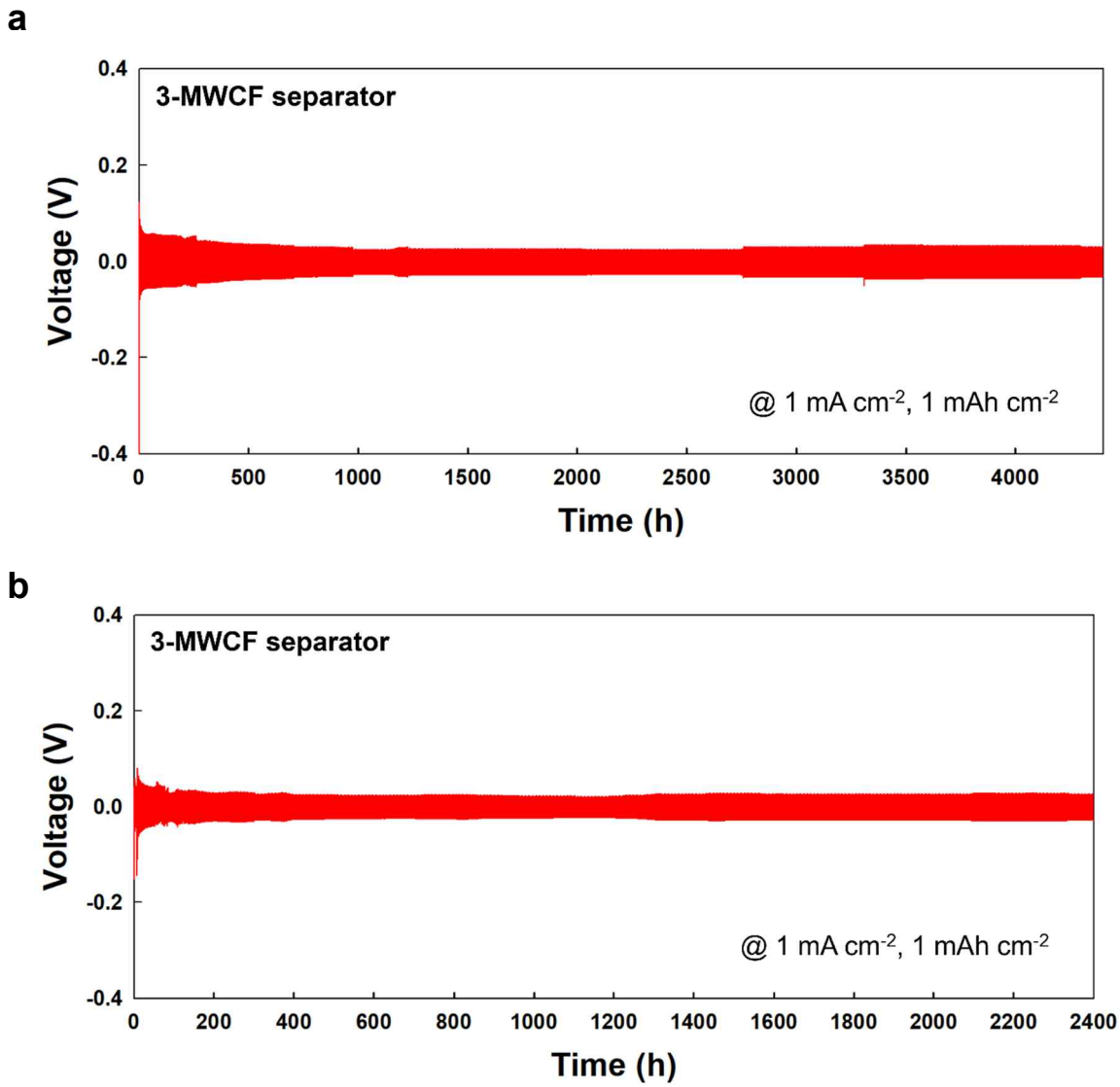


**Figure S23.** Galvanostatic cycling of 3-MWCF separator-based Li symmetric cells under 1 mA $cm^{-2}$, 1 mAh $cm^{-2}$ for a) 4400 and b) 2400 cycles. The consistent average overpotential and stable performance retention confirm the reproducibility and reliability of the *n*-MWCF separator systems (see **Figure 4e**). Additionally, among the repeatedly measured data, the most representative (or optimal) result was presented in **Figure 4e.**.

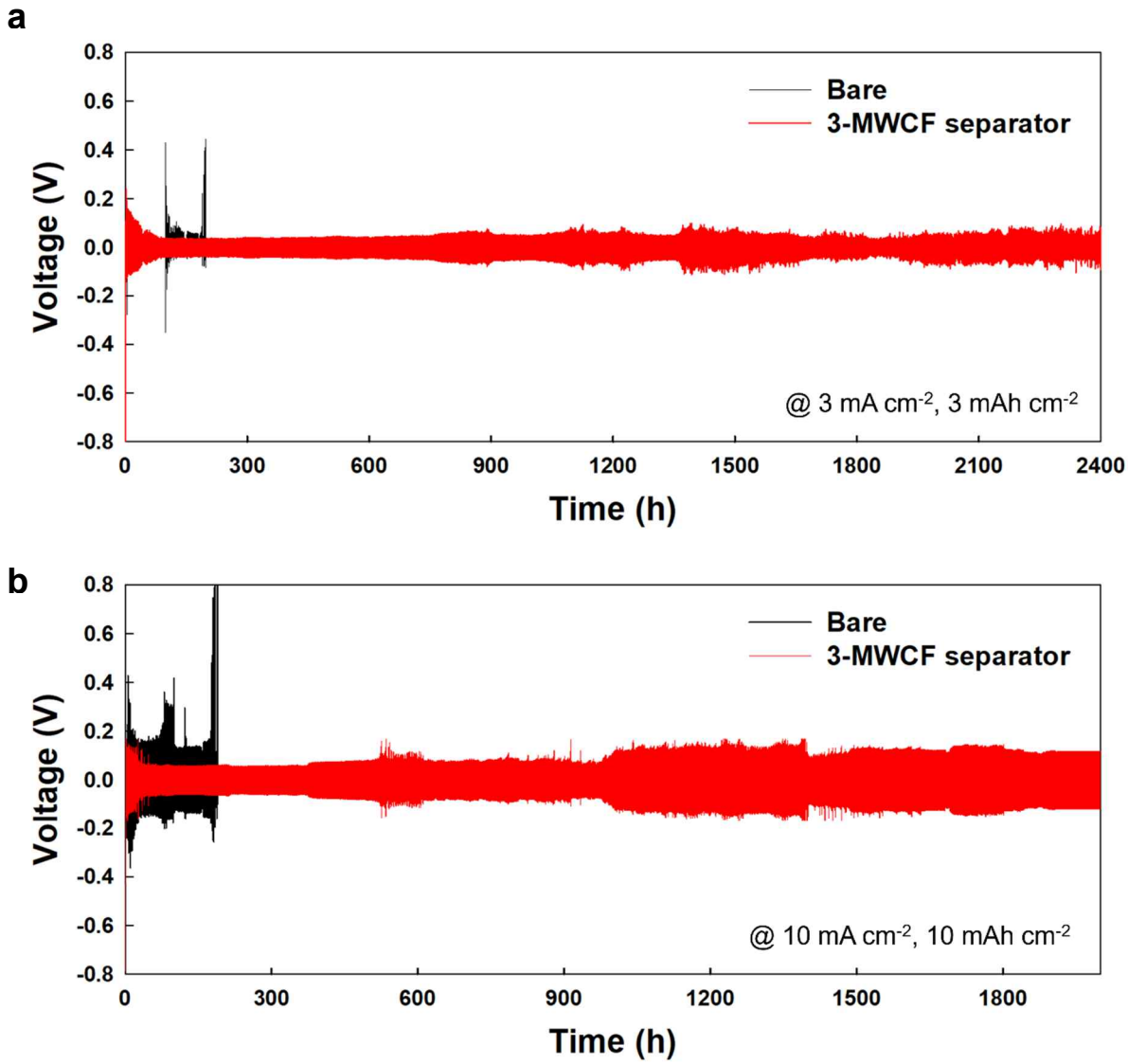


**Figure S24.** Symmetric cell stability test. Voltage (V) vs. time (h) profiles of 3−MWCF separator-based cells at a) 3 mA $cm^{-2}$/3 mAh $cm^{-2}$ and b) 10 mA $cm^{-2}$/10 mAh $cm^{-2}$.

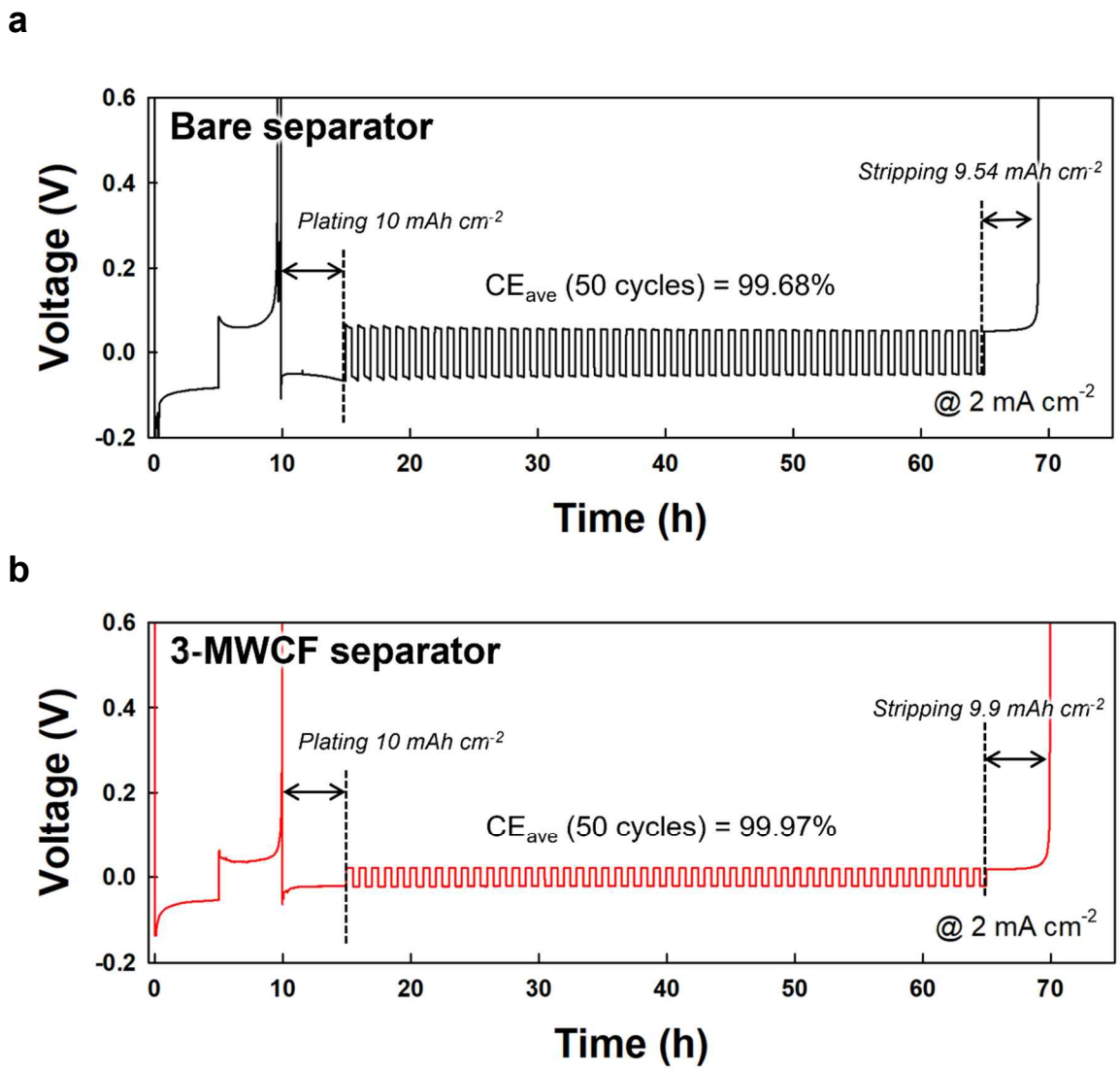


**Figure S25.** Average Coulombic efficiency. The average Coulombic efficiency measurements for a) bare and b) 3-MWCF separator at 2 mA $cm^{-2}$ and 1 mAh $cm^{-2}$ for 50 cycles, based on the modified test protocol proposed by Zhang and co-workers.[S8]

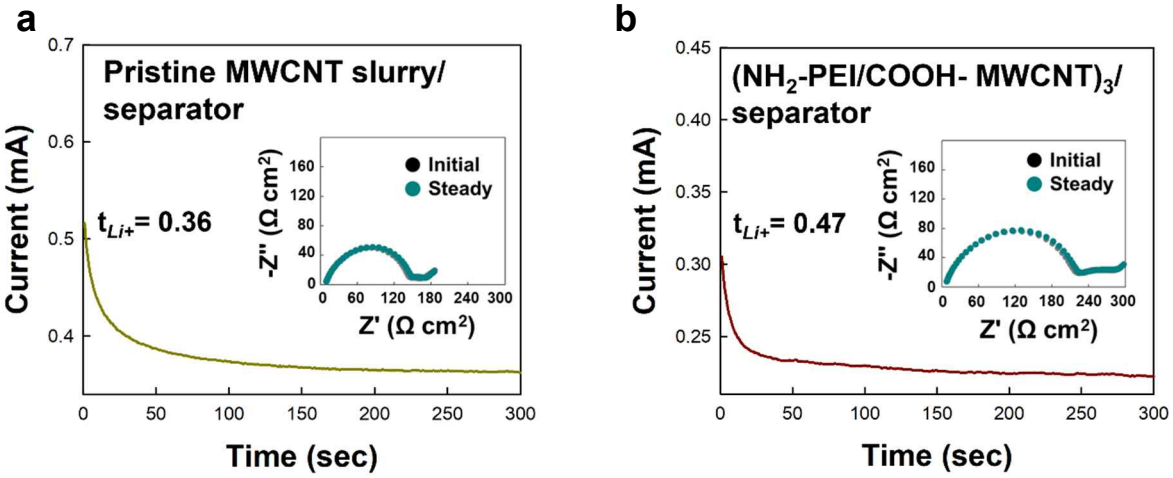


**Figure S26.** Chronoamperometry and EIS measurements. DC polarization profiles and EIS spectra (inset) for Li symmetric cells assembled using a) pristine MWCNT slurry-coated separator and b) $(NH_2$-PEI/COOH-MWCNT$)_3$-coated separator. In this case, the $Li^+$ ion transference number ($t_{Li+}$) of each cell was calculated to be 0.36 for slurry-based cell and 0.47 for $(NH_2$-PEI/COOH−MWCNT$)_3$-based cell, respectively.

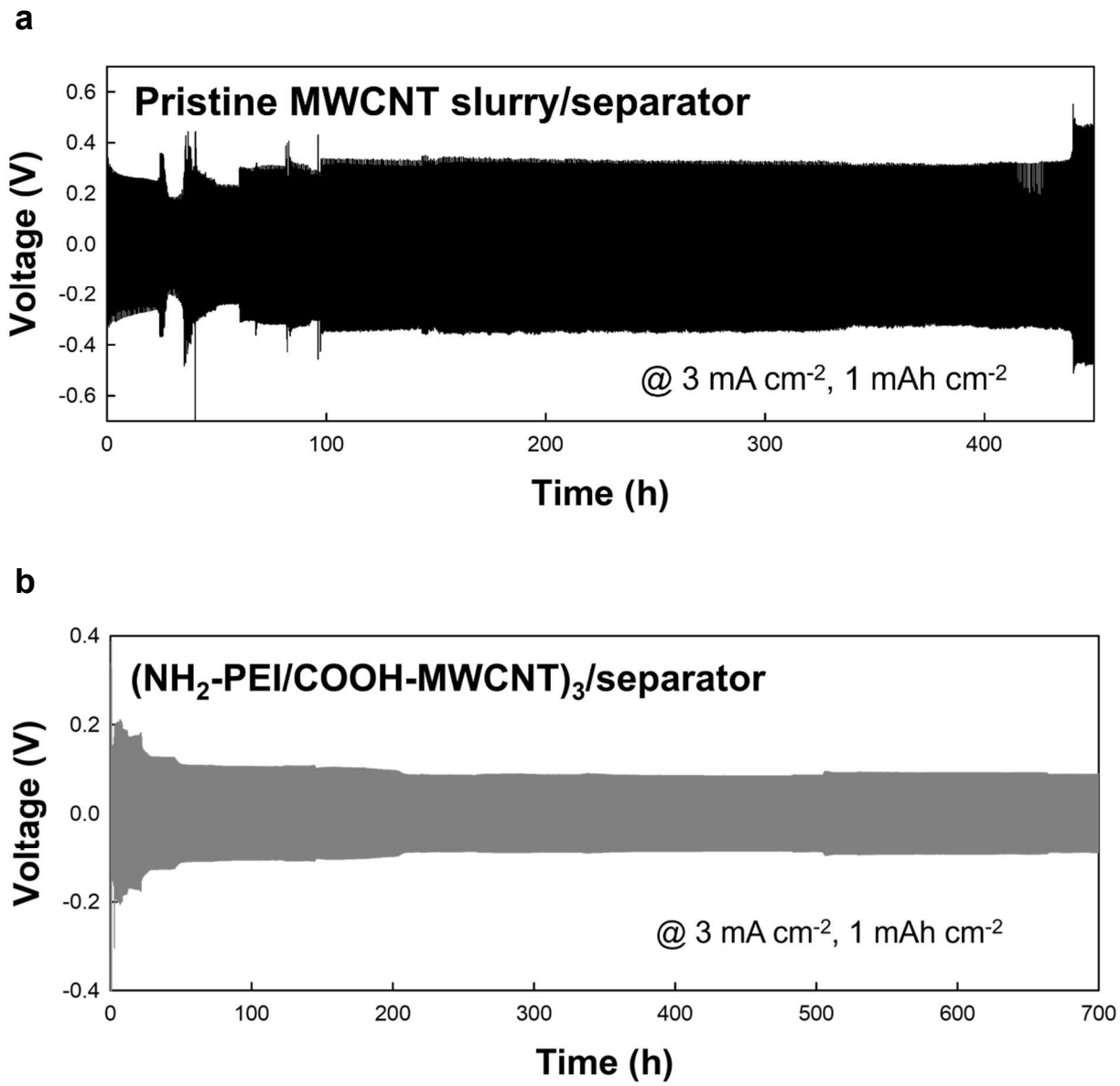


**Figure S27.** Cycle stability test. Voltage (V) vs. time (h) profiles of Li symmetric cells based on a) pristine MWCNT slurry-coated separator and b) $(NH_2\text{-PEI/COOH-MWCNF})_3$-coated separator at 3 mA $cm^{-2}$ and 1 mAh $cm^{-2}$. The MWCNT slurry-based cell showed heavy fluctuations of overpotential during the first 150 cycles, then maintained a high value of approximately 463.3 mV, suggesting poor ionic conduction behavior at the interfaces. In the case of the polymer linker ($NH_2$−PEI)-based interlayer, the overpotential was measured to be approximately 91.8 mV, which is much higher than that of TAA molecular linker-based interlayers. This is mainly due to the relatively high interfacial resistance of the $(NH_2$−PEI/COOH-MWCNT$)_3$ interlayer, which results in the formation of an unstable passivation layer (SEI) and impedes easy ion conduction at the interfaces.

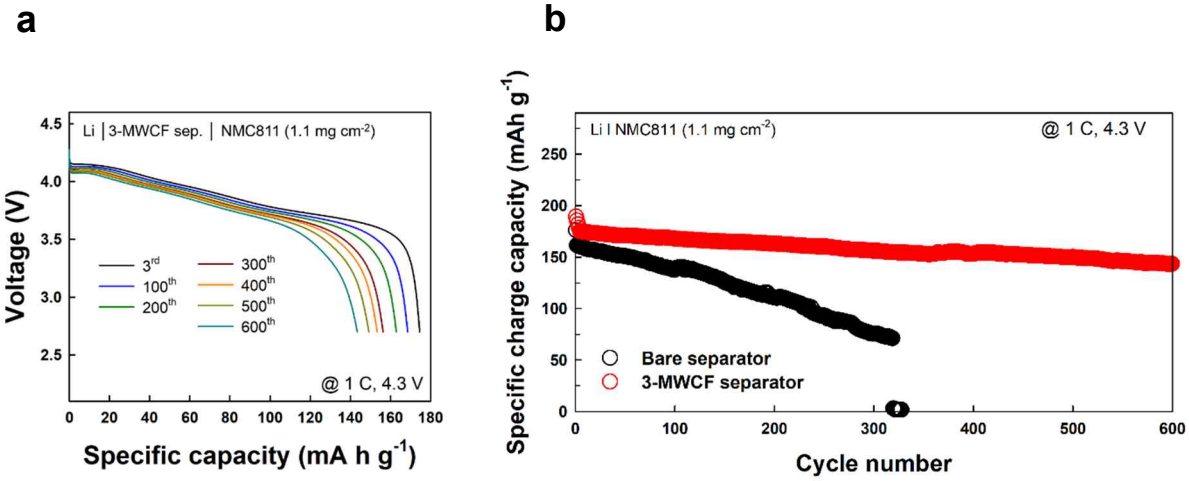


**Figure S28.** Galvanostatic charge/discharge (GCD) test. (a) Galvanostatic discharge profiles of 3−MWCF separator-based full cells as a function of cycle number. (b) Charge capacities of Li | NMC811 cells with 3−MWCF separator and bare separator.

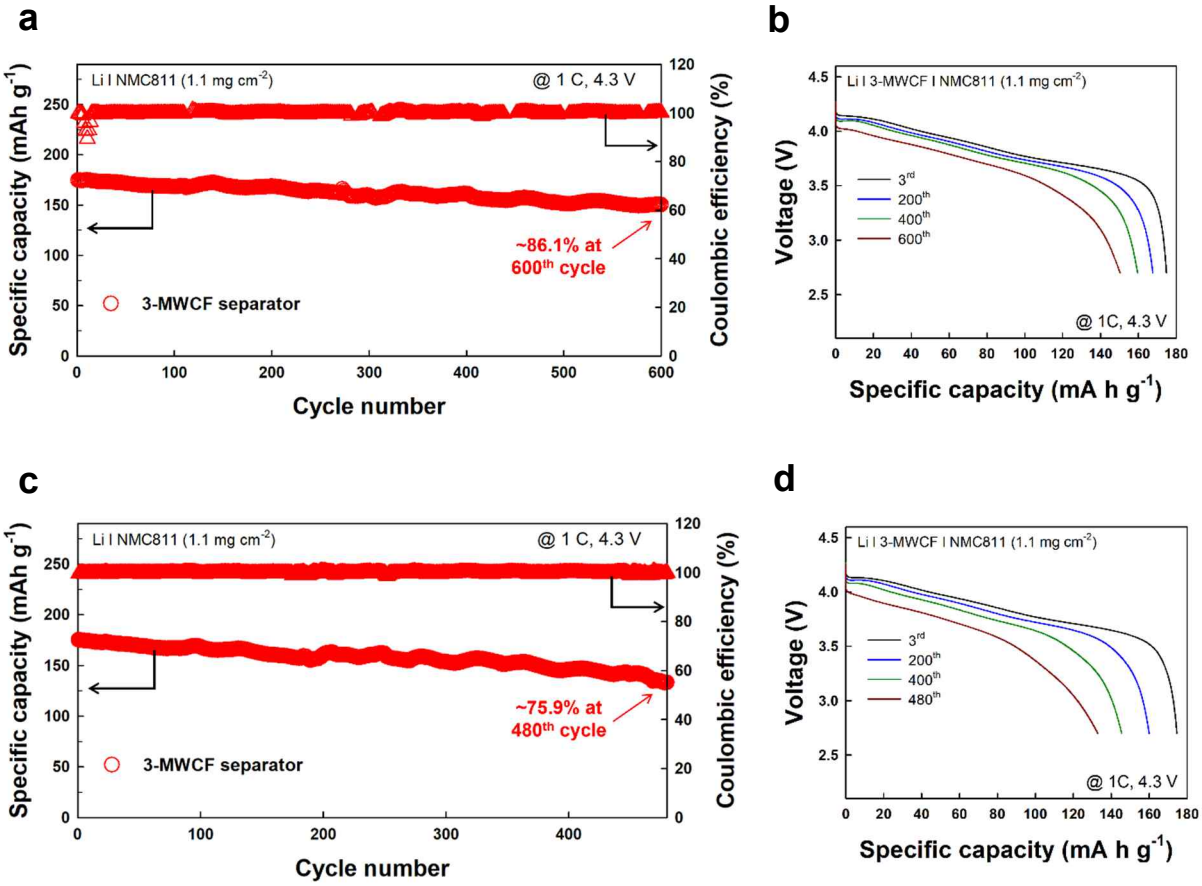


**Figure S29.** a, c) Galvanostatic cycling and b, d) corresponding voltage profiles of Li | NMC811 full cells. These data were obtained to confirm the reproducibility of the results presented in **Figure 5a**. These data were obtained to confirm the reproducibility of the results presented in **Figure 5a**. Additionally, among the repeatedly measured data, the most representative (or optimal) result was presented in **Figure 5a.**

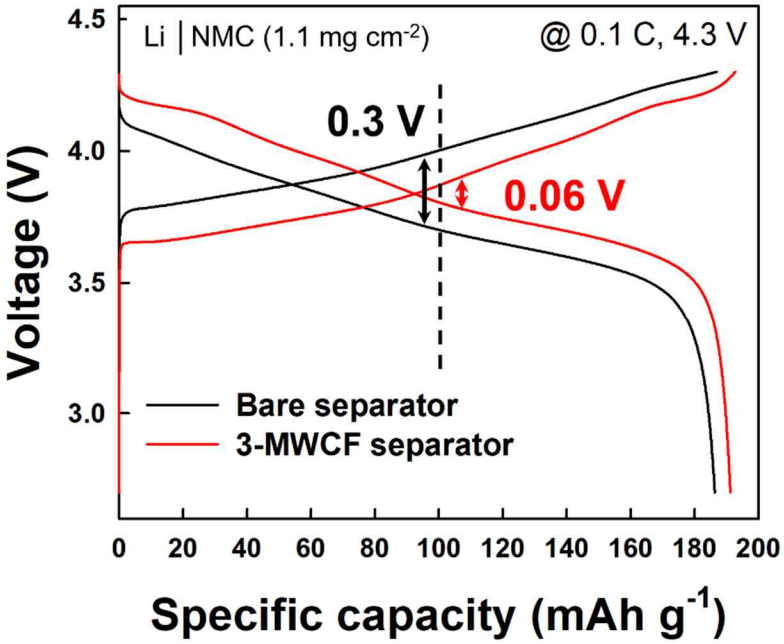


**Figure S30.** Galvanostatic charge/discharge (GCD) test. 5$^{th}$ GCD cycles of bare separator- and 3−MWCF separator-based asymmetric full cells at 0.1 C. The overpotential values of each cell were measured to be 0.3 V and 0.06 V, respectively.

a

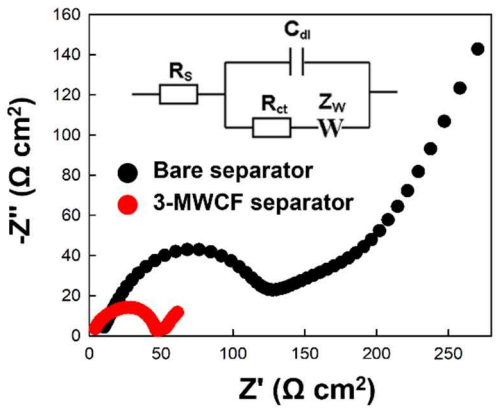


b

| | Bare separator | 3-MWCF separator |
|---|---|---|
| $R_s$ | 13.3 | 5.66 |
| $R_{ct}$ | 163.4 | 59.6 |

**Figure S31.** EIS measurement. a) Nyquist plots and simplified equivalent circuit (inset) of Li//LFP full cells assembled using bare separator (black solid circle) and 3−MWCF separator (red solid circle). b) Fitted impedance values of each cell.

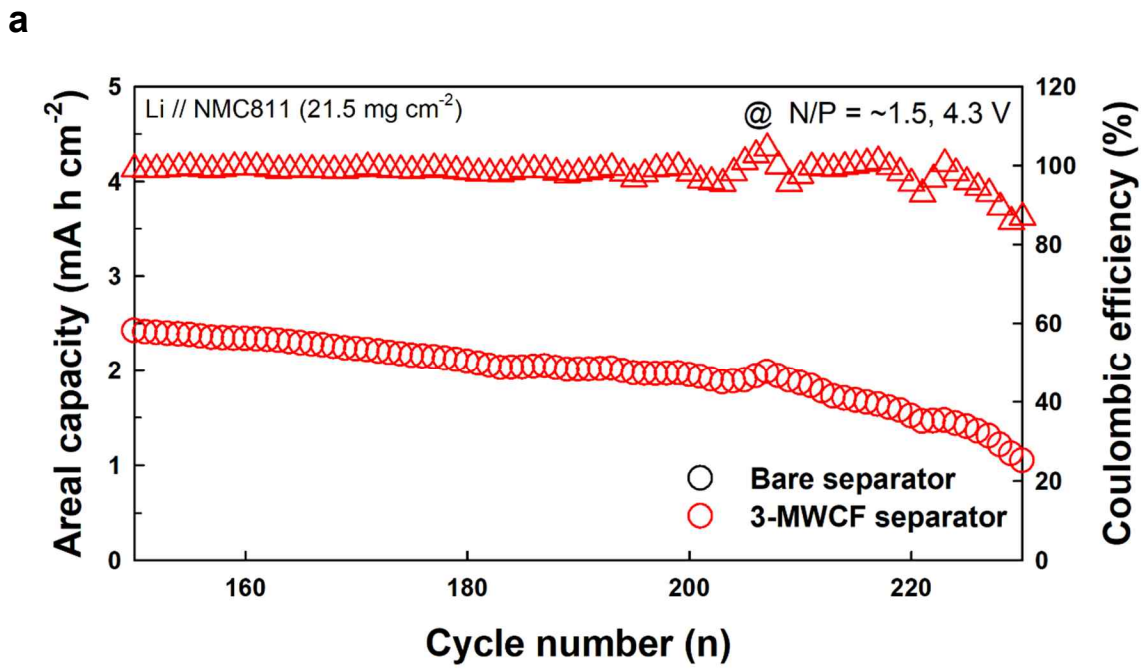


**Figure S32.** Performance of asymmetric full-cell with *n*-MWCF separator. Cycling trend of Li | NMC811 full cells with 3−MWCF separators after 150 cycles.

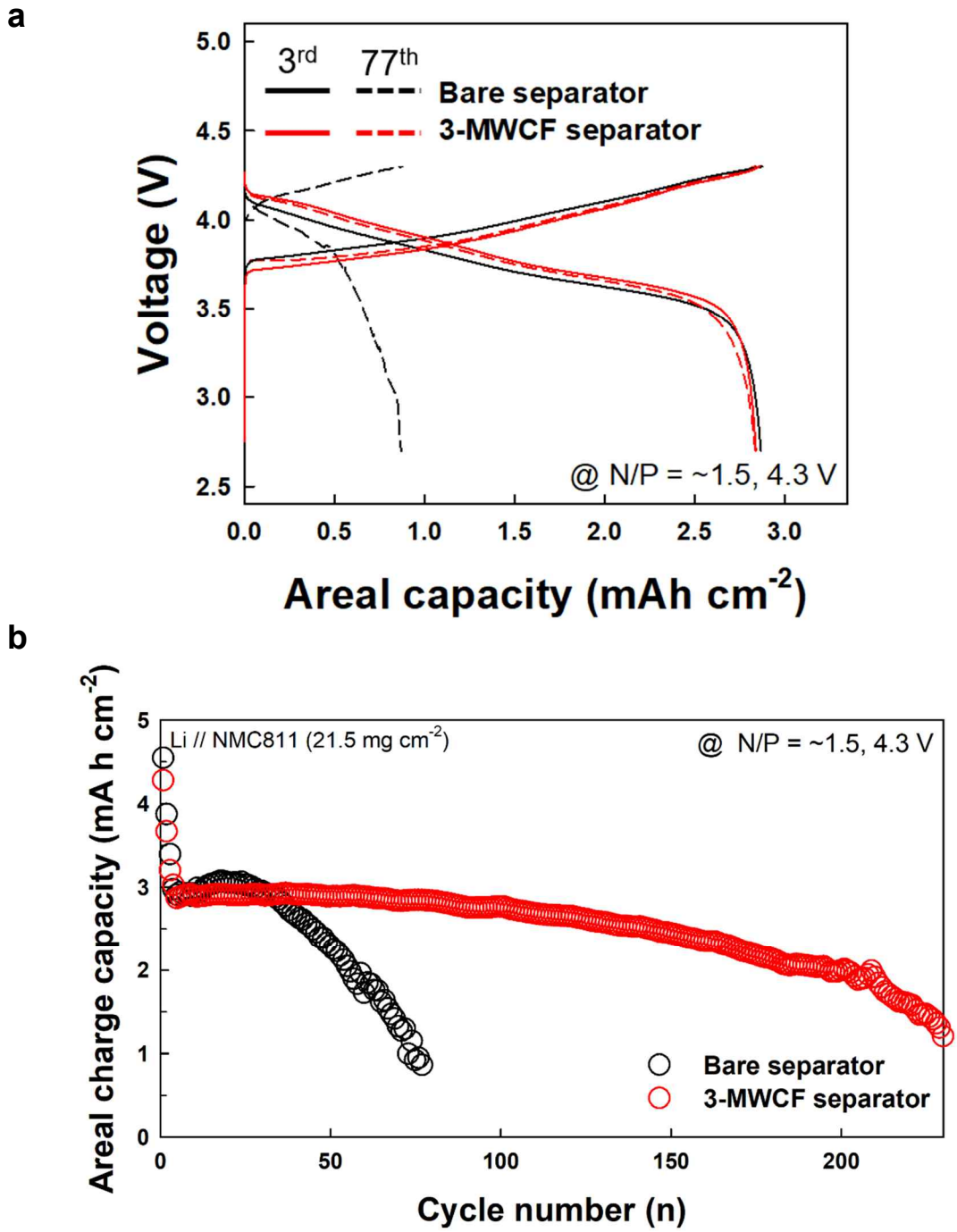


**Figure S33.** Galvanostatic charge/discharge (GCD) test. (a) Galvanostatic charge/discharge profiles and (b) charge capacities of Li | NMC811 (mass loading of 21.5 mg $cm^{-2}$) full cells with bare and 3−MWCF separators.

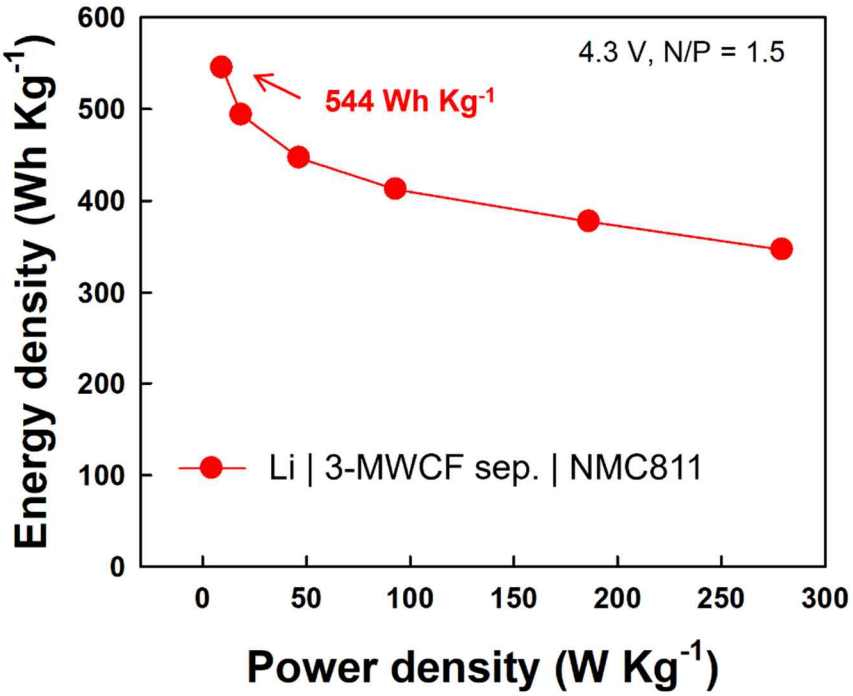


**Figure S34.** Energy and power densities. Energy and power densities of NMC811 (21.5 mg $cm^{-2}$)-based asymmetric cells at varying current densities. All values were obtained based on the weight of all electrode components, including the active materials, electrolyte, Al current collector, separator, and/or MWCF interlayer.

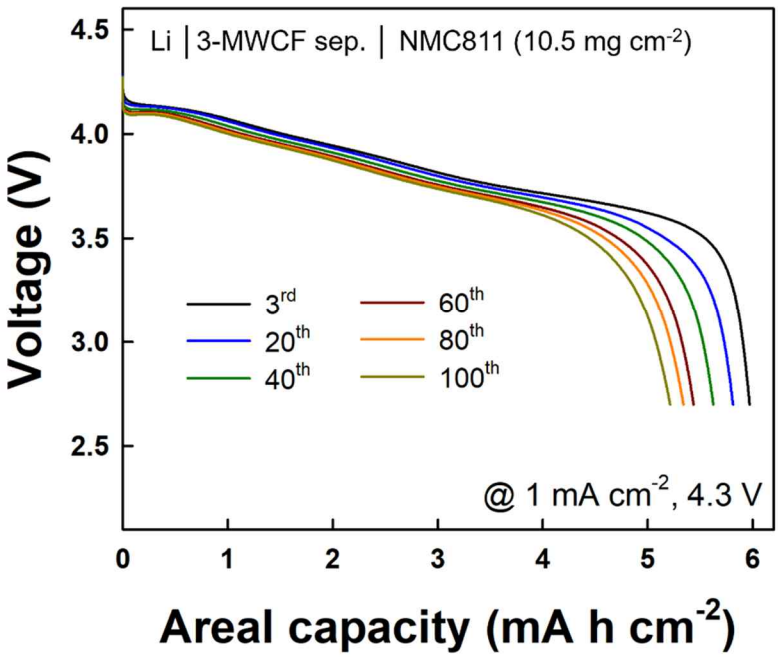


**Figure S35.** Galvanostatic charge/discharge (GCD) test. Discharge profiles of Li | NMC811 pouch cells with a cathode loading of 10.5 mg $cm^{-2}$, tested at 1 mA $cm^{-2}$.

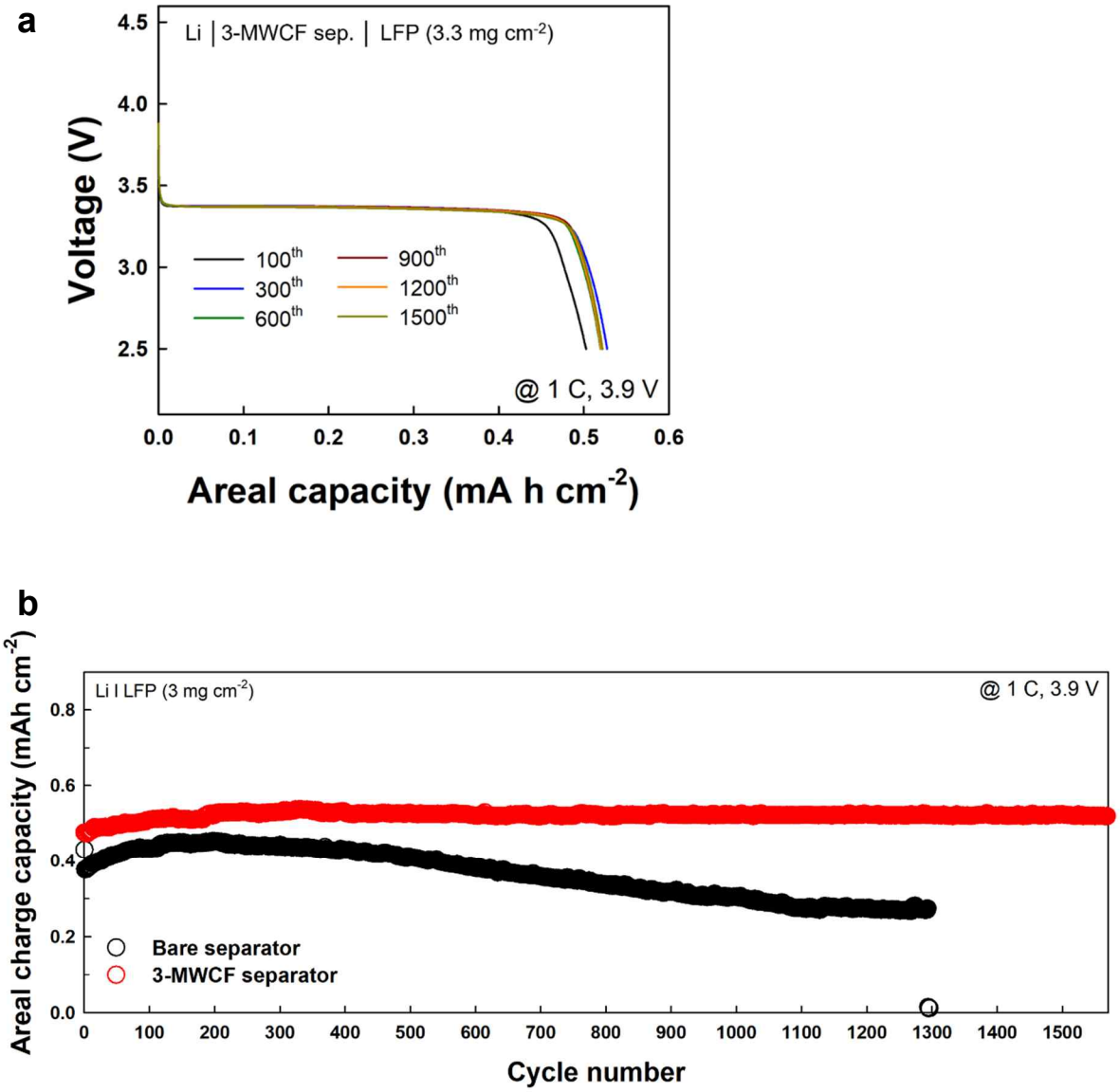


**Figure S36.** Galvanostatic charge/discharge (GCD) test. (a) Discharge profiles of Li | LFP cells with 3−MWCF separator, tested at 1 C. (b) Charge capacities of Li | LFP cells with 3−MWCF separator and bare separator.

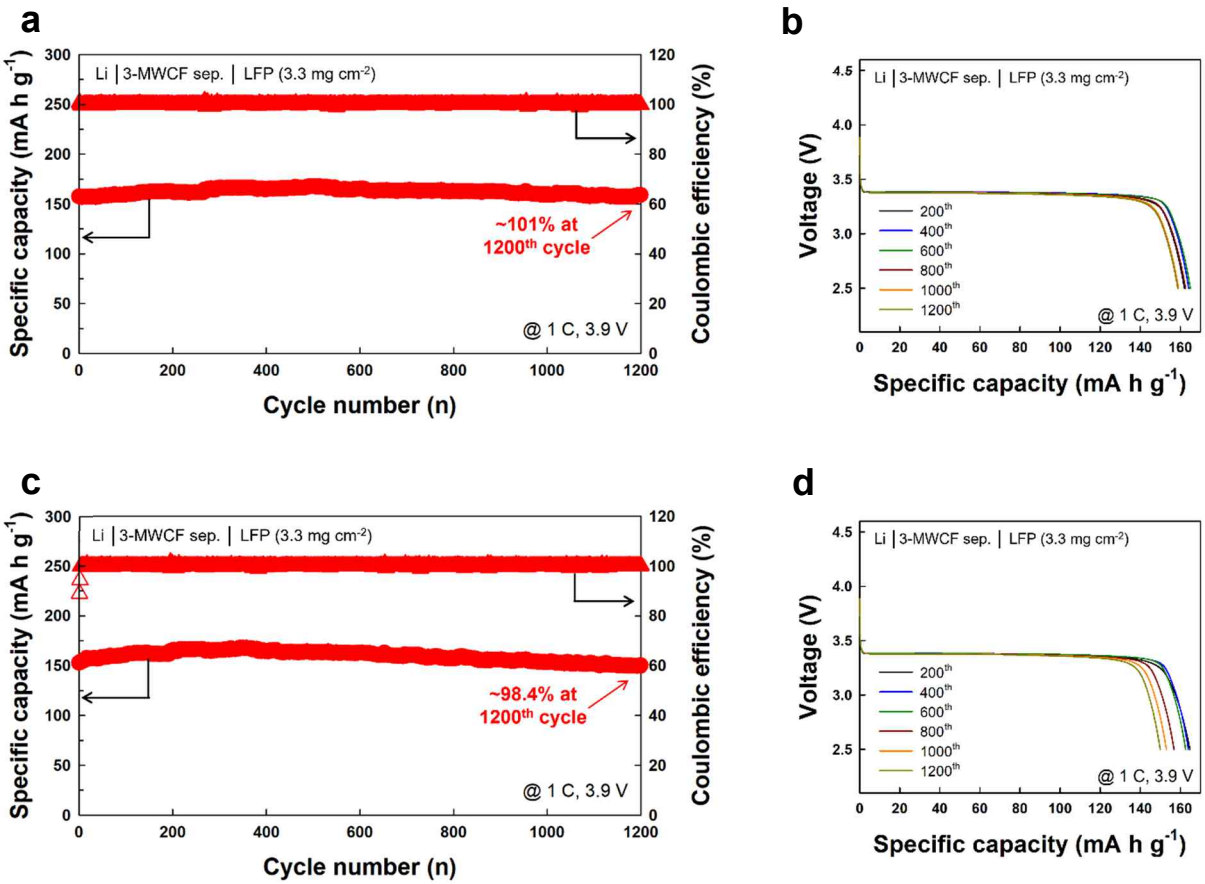


**Figure S37.** a, c) Galvanostatic cycling and b, d) corresponding voltage profiles of Li | LFP full cells. These data were obtained to confirm the reproducibility of the results presented in **Figure 5g**. Additionally, among the repeatedly measured data, the most representative (or optimal) result was presented in **Figure 5g.**

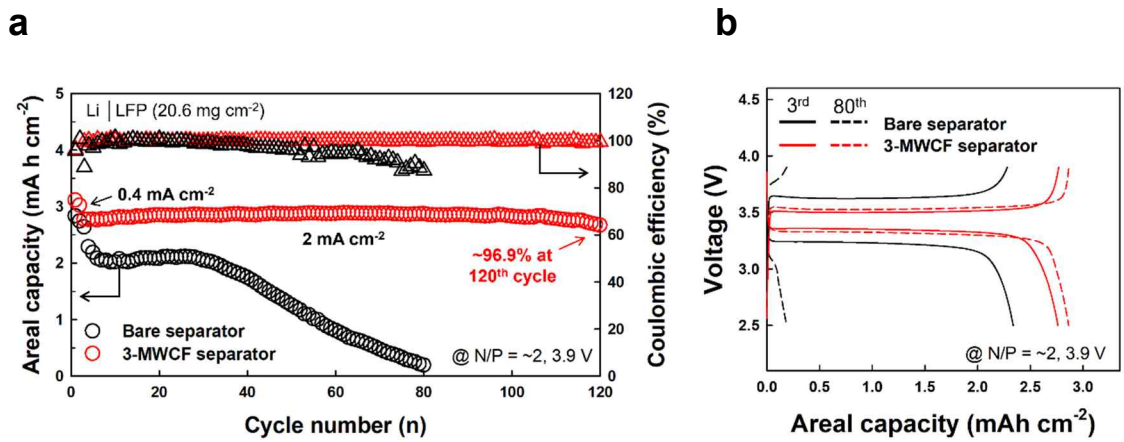


**Figure S38.** Capacity retention. a) Capacity retentions and b) corresponding galvanostatic charge/discharge profiles of Li | LFP full cells with bare and 3−MWCF separators.

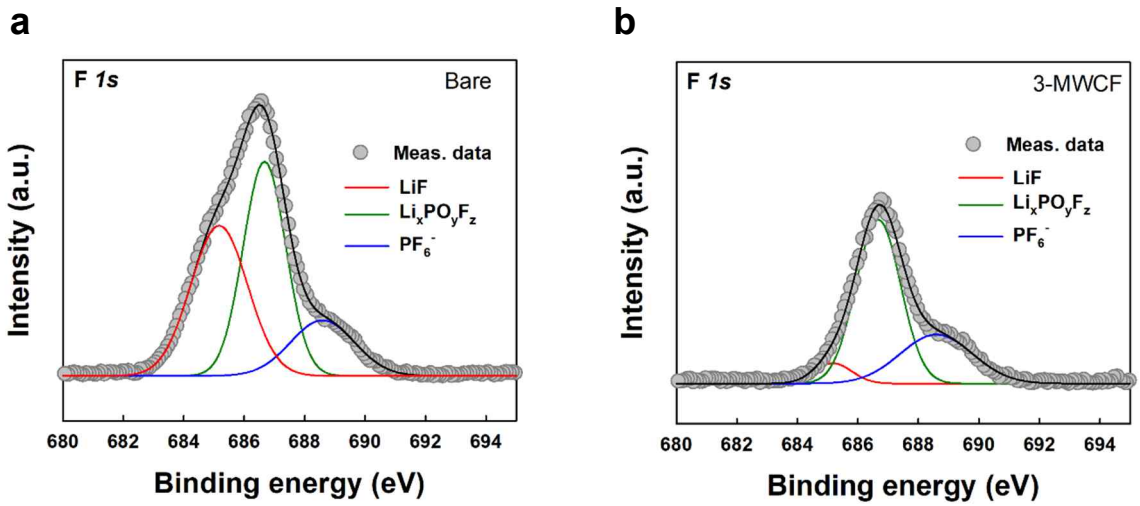


**Figure S39.** XPS analysis. XPS analysis of the F *1s* spectra was performed on the lithium metal anode from a) Li | bare separator | LFP and b) Li | 3−MWCF separator | LFP cells after the 100$^{th}$ discharge cycle. The deconvoluted F *1s* spectra for both separators revealed three distinct peaks at 685.1 eV, 686.6 eV, and 688.6 eV, corresponding to $PF_6^-$, LiF, and $Li_xPO_yF_z$, respectively. Notably, the lithium metal anode paired with the 3−MWCF separator exhibited lower intensities for LiF and $Li_xPO_yF_z$ compared to the bare separator. This reduction indicates the formation of a thinner and more uniform SEI layer, attributed to the homogeneous $Li^+$ ion flux facilitated by the 3−MWCF separator.

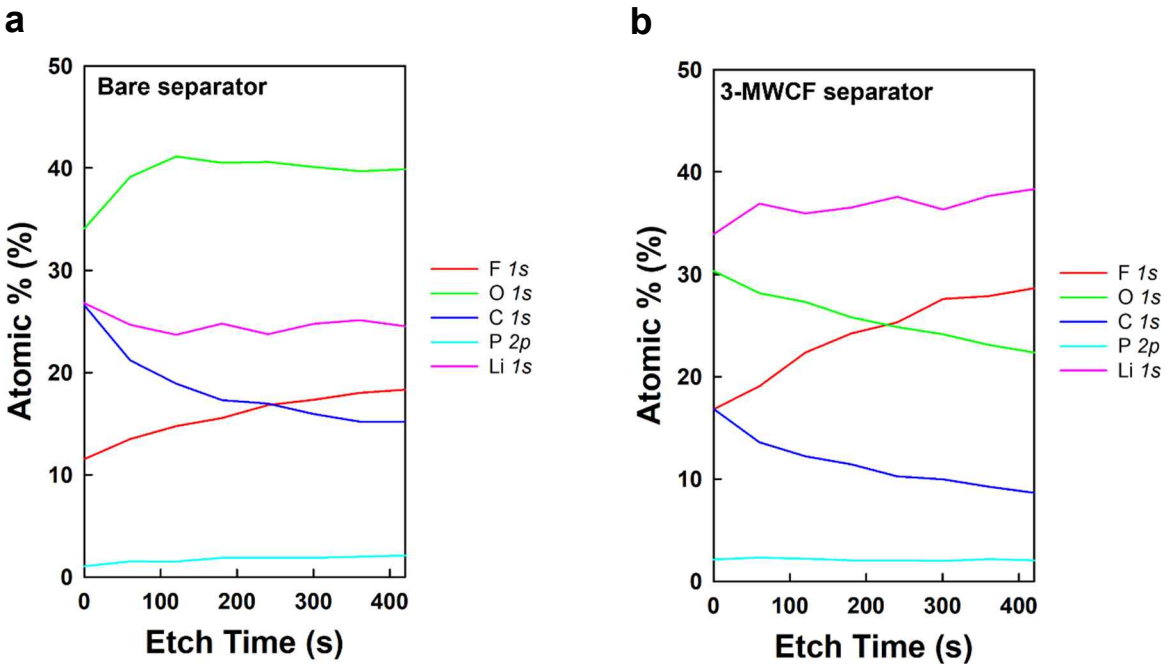


**Figure S40.** XPS depth profiles of the SEI layer in the Li//LFP full cells assembled with (a) a bare separator and (b) a 3-MWCF-coated separator. The 3-MWCF-based cell exhibited a relatively higher atomic percentage (%) of F 1s across the entire depth profiles, while the atomic contents of the other elements were lower compared to the bare separator-based cell. Typically, the F species are indicative of LiF formation within the SEI layer, a highly stable inorganic phase known to contribute to the mechanical and chemical stability of the electrode/electrolyte interface.

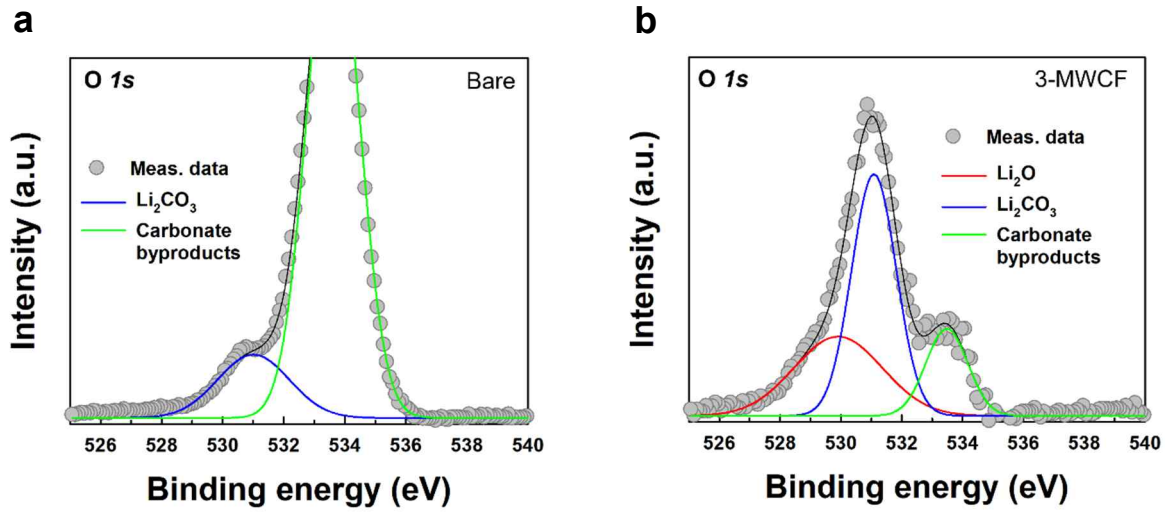


**Figure 41.** Deconvoluted O 1s and C 1s XPS spectra of Li//LFP full cells assembled with (a) a bare separator and (b) an MWCF-coated separator after 100$^{th}$ charge-discharge cycles. the deconvoluted O 1s XPS spectrum of the cell with MWCF-coated separator exhibits distinct peaks at 528.5 and 532.0 eV, corresponding to $Li_2O$ and $Li_2CO_3$, respectively—both of which are stable inorganic compounds typically formed in carbonate electrolyte-based systems.

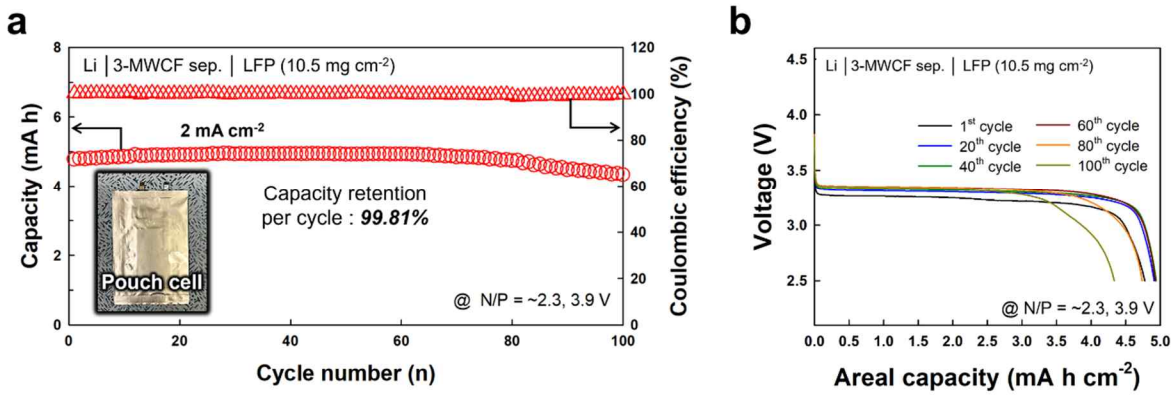


**Figure S42.** Capacity retention. a) Capacity retention and b) discharge profiles of Li | LFP pouch cells with a cathode loading of 10.5 mg $cm^{-2}$, tested at 2 mA $cm^{-2}$.

| Interlayer material | Method | Thickness | Li\|Li symmetric cell performance | Full cell performance | Ref. |
|---|---|---|---|---|---|
| 3-MWCF | Layer-by-layer assembly | ~60 nm | ~10,000 h @ 1 mA $cm^{-2}$<br>~7,000 h @ 3 mA $cm^{-2}$ | NMC811: 77.5% @800 cycles<br>LFP: 109% @1570 cycles | Our work |
| Poly(dimethylaminomethyl styrene) solvogel | Initiated chemical vapor deposition (iCVD) | 100 nm | ~820 h @ 1 mA $cm^{-2}$ | NMC622: 48% @650 cycles | [S9] |
| Crosslinked pressure-sensitive adhesive (70cPSA) | Radical copolymerization | ~4 μm | ~2,500 h @ 1 mA $cm^{-2}$<br>~1,500 h @ 2 mA $cm^{-2}$ | LFP: 93% @250 cycles | [S10] |
| Crosslinked polymer SEI | Polymer grafting | ~1 μm | ~1300 h @ 3 mA $cm^{-2}$ | Li-S: ~60% @500 cycles | [S11] |
| Boronic ester crosslinked polymer | Thiol-ene click chemistry | 1.49 μm | ~3500 h @ 1 mA $cm^{-2}$<br>~500 h @ 5 mA $cm^{-2}$ | LFP: ~94.2% @ 300 cycles (0.5 C)<br>~92% @ 300 cycles (1 C) | [S12] |
| SHIPN | Copolymerization | ~30 μm | ~500 h @ 3 mA $cm^{-2}$ | LFP: ~85.6% @ 500 cycles | [S13] |
| Lithiated graphite lamina with carbon coating | Slurry coating | 250 μm | - | NMC811: ~54% @300cycles | [S14] |
| NCF/rGO/$Li_3N$ hybrid layer | In situ formation on GO film | 10~50 μm | ~1500 h @ 1 mA $cm^{-2}$ | NMC811 (pouch): 93.5% @60 cycles | [S15] |
| Defective carbon collector (anode-free) | Carbonization of ZIF-8 on carbon paper | ~74 μm | - | NMC811: 90% @50 cycles | [S16] |
| Li-grafted graphene oxide in PVDF-HFP | Covalent grafting & casting | ~50 μm | ~720 h @ 0.5 mA $cm^{-2}$ | NMC811 (pouch): 78.4% @150 cycles | [S17] |

**Table S1.** Comparison of the electrochemical performance of various interlayers, including 3-MWCF, conventional carbon materials and polymer coatings.

**References**

[S1] D. A. Buttry, *Adv. Electroanal. Chem*., In electroanalytical chemistry, **1991**, *17*, 1.

[S2] E. Epifanovsky et al., Software for the frontiers of quantum chemistry: an overview of developments in the Q-Chem 5 package, *J. Chem. Phys.*, **2021**, *155*, 084801.

[S3] A. D. Becke, Density-functional exchange-energy approximation with correct asymptotic behavior, *Phys. Rev. A*., **1988**, *38*, 3098.

[S4] W. J. Hehre, R. Ditchfield, J. A. Pople, Self-consistent molecular orbital methods. XII. Further extensions of Gaussian-type basis sets for use in molecular orbital studies of organic molecules, *J. Chem. Phys*., **1972**, *56*, 2257-2261.

[S5] C. A. Schneider, W. S. Rasband, K. W. Eliceiri, NIH Image to ImageJ: 25 years of image analysis, *Nat. Methods*, **2012**, *9*, 671.

[S6] X. Chen, X. Wang, D. Fang, A review on C1s XPS-spectra for some kinds of carbon materials, *Nanotubes and Carbon Nanostructures*, **2020**, *28*, 1048.

[S7] C. Yan, X. Cheng, X. Y. Tian, X. T. Tian, J. Liu, J. Q. Huang, Q. Zhang, Lithium nitrate solvation chemistry in carbonate electrolyte sustains high-voltage lithium metal batteries, *Angew. Chem. Int. Ed.*, **2018**, *57*, 14055.

[S8] B. D. Adams, J. Zheng, X. Ren, W. Xu, J.-G. Zhang, Accurate determination of Coulombic efficiency for lithium metal anodes and lithium metal batteries, Adv. Energy Mater. **2018**, *8*, 1702097.

[S9] J. Bae, K. Choi, H. Song, D. H. Kim, D. Y. Youn, S.-H. Cho, D. Jeon, J. Lee, J. Lee, W. Jang, C. Lee, Y. Kim, C. Kim, J.-W. Jung, S. G. Im, I.-D. Kim, Reinforcing Native Solid-Electrolyte Interphase Layers via Electrolyte-Swellable Soft-Scaffold for Lithium Metal Anode, *Adv. Energy Mater.*, **2023**, *13*, 2203818.

[S10] S. Gao, Y. Pan, B. Li, M. A. Rahman, M. Tian, H. Yang, P.-F. Cao, Ultra-Stretchable, Ionic Conducting, Pressure-Sensitive Adhesive with Dual Role for Stable Li-Metal Batteries, *Adv. Funct. Mater.*, **2023**, *33*, 2210543.

[S11] Q. Wang, J. Yang, X. Huang, Z. Zhai, J. Tang, J. You, C. Shi, W. Li, P. Dai, W. Zheng, L. Huang, S. Sun, Rigid and Flexible SEI Layer Formed Over a Cross-Linked Polymer for Enhanced Ultrathin Li Metal Anode Performance, *Adv. Energy Mater.*, **2022**, *12*, 2103972.

[S12] C. Yang, H. Liu, M. Wang, H. Yan, J. Wang, R. Hu, Z. Wang, B. Zhou, Self-healing and robust polymer-based protective interlayer containing boronic esters for stabilizing lithium metal anode, *Chem. Eng. J.*, **2023**, *476*, 146580.

[S13] Y. Liu, X. Qin, F. Liu, B. Huang, S. Zhang, F. Kang, B. Li, Basal Nanosuit of Graphite for High-Energy Hybrid Li Batteries, *ACS Nano*, **2020**, *14*, 1837–1845.

[S14] H. Chen, W. Chen, D. Tian, L. Chen, X. Zhao, D. Mao, Y. Shen, F. Yu, Ultra-thin anodes with controlled thickness modified using *in situ* $Li_3N$ for high-energy-density lithium metal batteries, *J. Mater. Chem. A*, **2025**, *13*, DOI:10.1039/D5TA00725A.

[S15] H. Kwon, J.-H. Lee, Y. Roh, J. Baek, D. J. Shin, J.-K. Yoon, H. J. Ha, J. Y. Kim, H.-T. Kim, An electron-deficient carbon current collector for anode-free Li-metal batteries, *Nat. Commun.*, **2021**, *12*, 5537.

[S16] C. Shang, L. Cao, M. Yang, Z. Wang, M. Li, G. Zhou, X. Wang, Z. Lu, Freestanding $Mo_2C$-decorating N-doped carbon nanofibers as 3D current collector for ultra-stable Li–S batteries, *Energy Storage Mater.*, **2019**, *18*, 375–381.

[S17] F. Sun, Z. Li, S. Gao, Y. He, J. Luo, X. Zhao, D. Yang, T. Gao, H. Yang, P.-F. Cao, Self-Healable, Highly Stretchable, Ionic Conducting Polymers as Efficient Protecting Layers for Stable Lithium-Metal Electrodes, *ACS Appl. Mater. Interfaces*, **2022**, *14*, 26014–26023.